END
DATE
FILMED
1 84
DTIC

MICROCOPY RESOLUTION TEST CHART

NATIONAL BUREAU OF STANDARDS-1963-A

REPORT DOCUMENTATION PAGE		READ INSTRUCTIONS BEFORE COMPLETING FORM
1 REPORT NUMBER AFIT/CI/NR 83-63T	2 GOVT ACCESSION NO A135382	3 RECIPIENT'S CATALOG NUMBER
4 TITLE (and Subtitle) Kinetic Energy in the Northern Hemisphere during the FGGE Year		5 TYPE OF REPORT & PERIOD COVERED THESIS/DISSERTATION
		6 PERFORMING ORG. REPORT NUMBER
7 AUTHOR(s) Jeffrey Harold Zautner		8. CONTRACT OR GRANT NUMBER(s) -
9 PERFORMING ORGANIZATION NAME AND ADDRESS AFIT STUDENT AT: University of Wisconsin-Madison		10. PROGRAM ELEMENT PROJECT, TASK AREA & WORK UNIT NUMBERS
11. CONTROLLING OFFICE NAME AND ADDRESS AFIT/NR WPAFB OH 45433		12. REPORT DATE 1983
		13. NUMBER OF PAGES 72
14 MONITORING AGENCY NAME & ADDRESS(if different from Controlling Office)		15. SECURITY CLASS. (of this report) UNCLASS
		15a. DECLASSIFICATION DOWNGRADING SCHEDULE

16. DISTRIBUTION STATEMENT (of this Report)

APPROVED FOR PUBLIC RELEASE; DISTRIBUTION UNLIMITED

17. DISTRIBUTION STATEMENT (of the abstract entered in Block 20, if different from Report)

18. SUPPLEMENTARY NOTES

APPROVED FOR PUBLIC RELEASE: IAW AFR 190-17

2 1 Nov 83

LYNN E. WOLAVER
Dean for Research and
Professional Development

19 KEY WORDS (Continue on reverse side if necessary and identify by block number)

20. ABSTRACT (Continue on reverse side if necessary and identify by block number)

ATTACHED

DTIC
ELECTE
DEC 0 6 1983
E

DD FORM 1473 1 JAN 73   EDITION OF 1 NOV 65 IS OBSOLETE

UNCLASS

KINETIC ENERGY IN THE NORTHERN HEMISPHERE

DURING THE FGGE YEAR

by

JEFFREY HAROLD ZAUTNER

A thesis submitted in partial fulfillment of the
requirements for the degree of

MASTER OF SCIENCE
(Meteorology)

at the

UNIVERSITY OF WISCONSIN--MADISON

1983

ABSTRACT

Northern Hemisphere kinetic energy during the FGGE year is calculated on a twice daily basis at 0000 GMT and 1200 GMT. Graphs of time series of total (K), zonal (K_Z) and eddy (K_E) kinetic energy exhibit a strong annual cycle with superimposed short term fluctuations of about 14 to 16 days in K and K_E. This is confirmed by spectral analysis. Division of K_E into standing and transient components by month shows good agreement with values from Peixoto and Oort (1974) for standing K_E but poorer agreement for transient K_E. A large portion of the difference is probably due to interpolation methods. Standing and transient K_E by month and latitude show standing maxima associated with persistent trough and ridge features, mean jet stream and summer monsoon. A single transient maximum located about 5 to 10° north of the jet-related standing maximum appears associated with cyclone activity. Geographical plots of grid point K showed Asian and North American east coast winter maxima near equal intensity. Lower than average North American temperatures enhanced baroclinicity, contributing to the stronger than average maximum. Spring reveals a collapsed North American maximum, and the signature of the Indian monsoon appears prominent in summer. Available potential energy (A) quantities from Min and Horn (1982) allow K to A ratios to be compared with those of Peixoto and Oort (1974).

ii
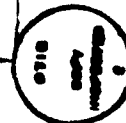
83 12 05 096

APPROVED: _Lyle H. Horn_

LYLE H. HORN

DATE: _5-10-83_

iii

TABLE OF CONTENTS

iv

ACKNOWLEDGEMENTS

v

1

1. INTRODUCTION

The sun is the primary source of energy to the earth and its
atmosphere. Within the atmosphere energy appears in various forms
with the transformations from one form to another of fundamental sign-
nificance to atmospheric processes. Of the various forms, kinetic
energy is of most direct importance to the meteorologist. As the
energy of motion, it is most directly related to weather producing
processes. Small vertical motions lead to cloud formation or dissi-
pation. Much larger horizontal motions provide the transport neces-
sary to maintain the global energy balance. As a scalar quantity,
kinetic energy cannot describe motion. Nevertheless, a knowledge
of it is essential in understanding the atmosphere's behavior, and
in particular, the atmospheric energy cycle. In this study kinetic
energy during the year of the First GARP Global Experiment (FGGE)
will be examined.

Over the years a great deal of research has been devoted to
kinetic energy, its budget, and its place in the atmospheric energy
cycle. For the most part, the research has fallen into three broad
categories: 1) kinetic energy budget studies over limited areas,
2) studies in the wave number domain, and 3) kinetic energy on a
hemispheric scale as part of the atmospheric energy cycle. Smith
(1980) provides an excellent overview of papers in the first area.
Saltzmann (1970) reviews earlier work in the wave number domain and
Tomatsu (1979) lists more recent research. Oort (1964) provides a

review of kinetic energy on a global/hemispheric scale in connection
with the atmospheric energy cycle. Peixoto and Oort (1974) and Oort
and Peixoto (1974, 1976) have performed extensive calculations of
energy generation, reservoirs, conversions and dissipation using
data covering a five year period. Although the work here does not
study the atmospheric energy cycle, it is most closely allied with
research in this third category. Thus, the Oort and Peixoto papers
provide material for comparison with kinetic energy values calculated
here.

This thesis will examine Northern Hemisphere kinetic energy
(K) during the FGGE year (December 1, 1978-November 30, 1979) in
considerable detail. Calculations are confined to the K of hori-
zontal motions since they are at least four orders of magnitude
larger than the K of vertical motions.* The study employs data in
isentropic coordinates so as to be compatible with the work of Min
(1981) and Min and Horn (1982), who compared available potential
energy (A) values computed using the exact formulation in isentropic
coordinates with the so-called approximate form developed in pres-
sure coordinates. The Northern Hemisphere K is examined with respect
to both its seasonal and geographical distributions. The total
kinetic energy (K) is partitioned into zonal kinetic energy (K_z) and
eddy kinetic energy (K_E), with the Ke divided into standing and

---

*In severe thunderstorms the vertical contribution might be nearly
 as large, but the larger scale focus and grid resolution employed
 here minimizes these contributions.

transient components. Time series analysis is employed to gain insight into the periodicity of the various K components. Using calculations from Min and Horn (1982), ratios of K to A are compared for the exact and approximate forms of A. Cross-spectral analysis of K and A are also done to gain some insight into the relationships between these energy forms during the FGGE year.

Chapters 2 and 3 contain a discussion of the basic data and calculation procedures, respectively. Following this, Chapter 4 presents the seasonal and geographical distributions of K and ratios of K to A. Chapter 5 presents the results of time series analysis. Chapter 6 contains a summary and suggestions for future work.

2. BASIC DATA

Unlike many previous studies of kinetic energy, the FGGE year
data does not rely on observations from only a limited number of
radiosonde stations. Several observing systems combine to provide
the best data set currently available for the entire globe.   The
FGGE data has been and will continue to be used by many researchers.
The use of this common data more readily allows for comparisons
between various studies. In particular, since comparisons are
planned between kinetic energy calculations of this study and the
available potential energy results from Min and Horn (1982) and Min
(1981), the choice of the same data period is crucial.

First consider a brief history of the basic data used here.
The National Meteorological Center (NMC) has been generating global
data sets on a twice daily basis for a number of years. Townsend
(1980) found that prior to September, 1978 the gridded analyses
generated by NMC's Hough spectral analysis procedure (Flattery, 1970)
contained numerous cases of superadiabatic layers. The wind analyses,
as expected, gave zonally-averaged meridional wind components that
were nearly zero. This effectively eliminated the Hadley and Ferrel
meridional circulations he hoped to find. Thus, Townsend was unable
to use the Hough gridded data. In September, 1978, in preparation
for a FGGE year, NMC introduced an optimum interpolation global
data assimilation system (Bergman, 1979; McPherson et al., 1979).
Townsend's subsequent testing showed only an occasional superadia-

batic layer, and the wind field now contained non-zero meridional wind components. Gridded data based on this scheme were used by Townsend (1980) and Min (1981) and will be employed in this study.

a. The FGGE level IIIa data set

The FGGE level IIIa data set used in this study was obtained from the National Center for Atmospheric Research (NCAR). The data include pressure, temperature, wind and relative humidity compiled twice daily at 0000 GMT and 1200 GMT. The data were arrayed in a 2.5° latitude-longitude grid for each of the 12 mandatory isobaric levels: 1000, 850, 700, 500, 400, 300, 250, 200, 150, 100, 70, and 50 mb. A heterogeneous collection of observing systems provided the raw information. The systems included conventional radiosonde observations (RAOBs), surface reports from land stations and ships and conventional aircraft reports (AIREPs). A unique feature of FGGE was the extensive coverage of data sparse oceanic regions by satellite. The geostationary satellite system generated cloud-tracked winds and a polar orbiting satellite, TIROS-N, yielded vertical temperature profiles. In tropical regions, two special systems provided observations: the Tropical Wind Observing Ships (TWOS) and Tropical Constant Level Balloons (TCLB). During the two FGGE Special Observing Periods of January-February and May-June, OMEGA-system dropsondes produced temperature, relative humidity and wind observations along specific aircraft routes primarily in the tropics. See Fleming et al. (1979a,b) for a more complete description of the

data set.

The variety of observing systems produced meteorological measurements with differing error characteristics. Consequently, NMC developed a data assimilation system based on a statistical interpolation scheme. The statistical method, an optimum interpolation (OI) analysis scheme, is capable of multivariate analysis of winds and temperatures. The OI scheme, which assumes that both observed and forecast values are subject to error, updates predicted values with observations. For the details of the NMC global assimilation system see Bergman (1979) and McPherson et al. (1979).

b. Isobaric-isentropic data processing

In processing the data, NMC generated the global analysis in sigma coordinates and then used vertical interpolation from sigma to isobaric coordinates to obtain the isobaric analysis. The processed Northern Hemisphere data were stored in 145x37 longitude-latitude arrays. This corresponds to a 2.5° longitude-latitude grid. Data arrays were generated for the 12 mandatory pressure levels from 1000 to 50 mb on a twice daily basis at 0000 GMT and 1200 GMT.

Of a possible 730 observation times during the FGGE year, 703 were available in the data set. Min (1981) eliminated two additional periods because of suspect data in his available potential energy study. While calculating kinetic energy, two more time periods were eliminated because of unrealistic wind values (in excess

of 1000ms^{-1}) at several grid points. Thus a total of 699 observation times were employed. Because the missing periods shown in Table 1 were about equally distributed throughout the 12 months, no attempt was made to interpolate for missing analyses.

Min (1981) made some initial calculations of available potential energy to test different horizontal and vertical resolutions. From his calculations it was decided to employ a 5° latitude-longitude grid and 10K isentropic vertical intervals. This study employs the same horizontal and vertical resolution.

Obtaining isentropic data from the NMC analyses proved to be a major undertaking. Townsend (1980) generated the isentropic data by vertical interpolation of mandatory level data to isentropic surfaces. He used an algorithm developed by T. Whittaker at the University of Wisconsin. The algorithm assumes a linear variation of pressure while all other parameters vary with $\theta^{1/\kappa}$. The ten mandatory pressure levels from 1000 to 100 mb were used in this interpolation. The top isentropic surface is at 370K, which corresponds roughly to the 150 mb level, and thus, includes essentially all of the tropospheric circulation. Potential temperature (θ) extends downward from 370K in 10K increments. The lowest θ surface present during a data period depends on the minimum observed potential temperature at the earth's surface at any grid point over the hemisphere. Values as low as 220K were observed during the winter. Thus, data from the ten mandatory pressure levels were interpolated to as many as 16 isentropic surfaces extending from 370K to as low as 220K.

Table 1. Distribution of the number of missing data in FGGE level

IIIa data set.

	0000 GMT	1200 GMT	Total
December, 1978	1	0 (2)*	1 (3)
January, 1979	1	1	2
February	1	0	1
March	2	1	3
April	1	1	2
May	0	2	2
June	1	3	4
July	0	1	1
August	1	1	2
September	4 (6)*	3	7 (9)
October	1	0	1
November, 1979	1	0	1
Total	14 (16)	13 (15)	27 (31)

*Two time periods in December were eliminated because of excessive winds at some grid points. The two additional periods eliminated in September resulted from very small A values found by Min (1981).

3. EQUATIONS AND COMPUTATIONAL METHODS

a. Kinetic energy equations

In this study, total kinetic energy (K) per unit area is defined as

$$K = \frac{-1}{2gS} \int_S \int_{\theta_s}^{\theta_t} (u^2 + v^2) \frac{\partial p}{\partial \theta} \, d\theta dS \qquad (1)$$

where g is gravitational acceleration, S is hemispheric surface area, u and v are, respectively, the eastward and northward components of the wind, p is pressure, θ is potential temperature and $dS = \dot{a}^2 \cos\phi d\phi d\lambda$, where a is the earth's radius, ϕ is latitude and λ is longitude. The vertical integration performed in isentropic coordinates extends from 220K to 370K.

K was partitioned into zonal (K_Z) and eddy (K_E) components:

$$K_Z = \frac{-1}{2gS} \int_S \int_{\theta_s}^{\theta_t} ([u]^2 + [v]^2) \frac{\partial p}{\partial \theta} \, d\theta dS \qquad (2)$$

$$K_E = \frac{-1}{2gS} \int_S \int_{\theta_s}^{\theta_t} (u^{*2} + v^{*2}) \frac{\partial p}{\partial \theta} \, d\theta dS \qquad (3)$$

where [ ] indicates a zonal average and ()* is the deviation from the zonal average. Appendix A contains detailed information on the actual computational procedures.

It is instructive to further divide K_E into its standing and transient components. The transient component of $\overline{K}_E$ ($\overline{K}_{Etr}$) may be written as

$$\overline{K}_{Etr} = \overline{K}_E - \overline{K}_{Est} \qquad (4)$$

where the overbar implies a time average. The subscripts tr and st identify the transient and standing components. $\overline{K}_{Est}$ is given by

$$\overline{K}_{Est} = \frac{-1}{2gS} \int_S \int_{\theta_s}^{\theta_t} (\overline{u^*}^2 + \overline{v^*}^2) \frac{\partial \overline{p}}{\partial \theta} d\theta dS \qquad (5)$$

In the above equation, isobaric data is first time averaged for each month and then interpolated to θ coordinates. This method is employed, rather than time averaging the twice daily isentropic data, since the height of a pressure surface fluctuates less than the height of an isentropic surface during a month.

The geographical distribution of K and its standard deviation is also investigated. Each 5° latitude-longitude box can be represented by its vertically integrated grid point value. Specific units (Jkg^{-1}) are employed because, when calculating the vertical integral in θ coordinates, the mass between θ_s and θ_t can vary from one point to another. The K equation in specific units is

$$K = \frac{\frac{-1}{2} \int_s \int_{\theta_s}^{\theta_t} (u^2 + v^2) \frac{\partial p}{\partial \theta} d\theta ds}{\int_s (P_{sfc} - P_{top}) ds} \qquad (6)$$

where the denominator represents the mass in the column determined

from the surface pressure and the pressure at the top of the domain,

i.e., P_{top} at 370K, and small s is the area of the grid box. See

Appendix A for a discussion of area calculation. The equations

for K_Z and K_E in specific units are similar to Equation 6. Note

that since the wind is broken into a zonal average and a deviation

at each grid point (e.g., $u = [u] + u^*$), a cross product term is

implicitly included in grid point values of K. For example, $u^2 =$

$[u]^2 + 2[u] u^* + u^{*2}$. Since $K_Z \alpha [u]^2$ and $K_E \alpha u^{*2}$, the cross product

term $2[u]u^*$ makes neither a zonal nor eddy contribution. The $2[u]u^*$

term integrates to zero in zonal rings and in the hemispheric total;

however, it is contained implicitly in the total K value at each

grid point. Thus, at grid points, K is not equal to the sum of K_Z

and K_E.

b. Time series analysis

A wealth of information about a time series can be readily ob-

tained by performing a Fourier analysis. The Fourier analysis fits

sine and cosine waves to the data to estimate the contribution of

each Fourier frequency to the actual time series. The variance ex-

plained by a particular Fourier frequency can be obtained from the

power (or variance) spectrum which is computed as

$$P_i = \frac{1}{2} (a_i^2 + b_i^2) \tag{7}$$

where each P_i gives the amount of variance explained by a particular Fourier frequency. By standardizing the data prior to analysis, P_i represents a percentage of total variance explained at the i'th frequency. The coefficients, a_i and b_i are given by

$$a_i = \frac{2}{N} \sum_{t=1}^{N} [X(t)\sin(i\omega t)]$$

$$b_i = \frac{2}{N} \sum_{t=1}^{N} [X(t)\cos(i\omega t)]$$

(8)

where i may be any integer from 1 to $\frac{N}{2} - 1$. The summation is over the N observations, and X(t) is the value of the series at point t. The frequency, ω, is equal to $2\pi/T$, where T is the period of record. By subjecting two simultaneous time series to spectral analysis, one learns how the two series vary together. This cross spectral analysis consists of two parts, the coincident spectrum (C) and the quadrature spectrum (Q). C measures the amount of the two series in-phase relation and Q measures the out-of-phase relation. The coincident and quadrature spectrums are given by

$$C_i = a_{xi} a_{yi} + b_{xi} b_{yi}$$

$$Q_i = b_{xi} a_{yi} - a_{xi} b_{yi}$$

(9)

where the subscripts denote the coefficients from the two simultaneous series X and Y for the i'th frequency. A phase angle difference ($\Delta\beta$) is computed from C and Q at each frequency as

$$\tan(\Delta\beta_i) = \frac{Q_i}{C_i} \tag{10}$$

Finally, to determine how good a relationship exists between the two series, the coherence (CH) is computed as

$$CH_i = \frac{C_i^2 + Q_i^2}{P_{xi} \cdot P_{yi}} \tag{11}$$

The coherence is estimated by summing over a finite band of frequencies. This is frequently done for estimating P as well since this increases the degrees of freedom for the spectral estimate. This will be discussed more completely in Chapter 5. Coherence can range from 0 to 1 and is analogous to the square of a correlation coefficient except that CH is a function of frequency.

A more complete discussion of spectral analysis can be found in Panofsky and Brier (1958) and Bendat and Piersol (1971). Additionally, Appendix B contains a discussion of the procedures employed prior to using a fast Fourier transform (FFT) to obtain the spectral results presented in Chapter 5.

4. RESULTS

This section presents the findings derived from the twice daily kinetic energy calculations performed for the Northern Hemisphere using the level IIIa FGGE data set. The time series of kinetic energy values are discussed first, followed by a more detailed look at K_E which is partitioned into its standing and transient components. Next, the spatial distribution of the mean seasonal K and its standard deviations are reviewed. Finally, ratios are calculated using A from Min and Horn (1982).

a. Time series of kinetic energy values

Figure 1 shows the twice daily values of the total kinetic energy (K) and its zonal (K_Z) and eddy (K_E) components vertically integrated from 220K to 370K over the area of the Northern Hemisphere. Units are $x10^5$ Jm^{-2}. All three curves exhibit a strong annual cycle which responds to the solar cycle, with the zonal term showing slightly more seasonal variation than the eddy term. This is in agreement with the findings of Peixoto and Oort (1974) and is what one expects from examining upper air charts over the course of a year. K is highest during the winter months when radiation differences are largest between the equator and pole. This leads to large north-south temperature contrasts, which yield strong zonal winds aloft via the thermal wind relationship. Excessively large thermal gradients and zonal winds would result were it not for the
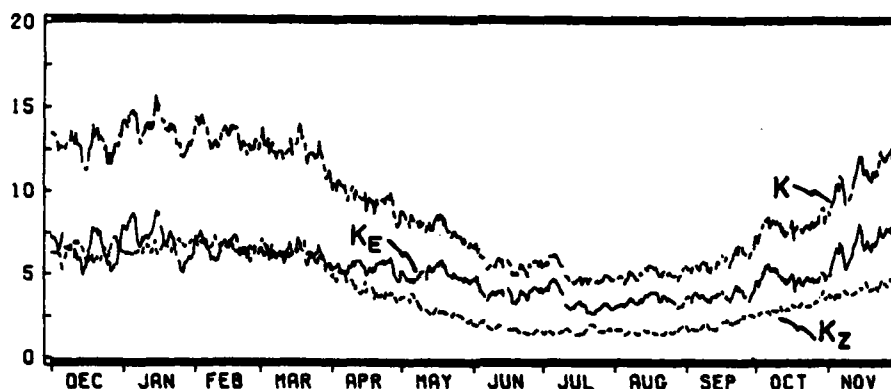
Figure 1. Time series of twice daily vertically integrated K for
the Northern Hemisphere during the FGGE year. Total
(dash-dot), zonal (dash) and eddy (solid). Units:
10^5 Jm^{-2}.

development of vigorous eddy motions which transport heat poleward.
The K curve exhibits a strong pulsing in the winter on the order of
12-16 days. This strong pulsing returns in late autumn when radia-
tion deficits in high latitudes are increasing. Visual inspection
shows that when K exhibits peaks, so does K_E; thus eddy motions appear
to be the primary contributor to the short term shape of the K
curve, while zonal motions tend to provide a quasi-steady background
state.

As spring approaches, a nearly steady decline in K begins and
extends through mid-summer. The decrease is most evident in K_Z.
This is a reflection of the decreasing baroclinicity between the
tropics and high latitudes. The decline in K_E is less pronounced.
East-west heating differences, which result in eddy motions, are

evidently becoming relatively more important and partly replace the vigorous winter-time eddies which are required for a poleward energy transport. Consequently, K_E decreases less than K_Z during the warmer seasons.

Summer is a period of low K values, but as autumn approaches, K begins to increase. The short period fluctuations return in K and K_E while K_Z slowly increases. Note that the FGGE year ended at a somewhat lower kinetic energy level than it began. The difference is made up almost entirely by lower levels of K_Z at year's end.

Monthly mean values of twice daily kinetic energy are shown in Figure 2. Monthly values are connected to show the overall trend from month to month. Note that the FGGE year begins with K_Z and K_E about equal and ends (November) with K_E significantly greater than K_Z. Figure 3 is identical to Figure 1 except that it shows the time series of 0000 GMT and 1200 GMT kinetic energy separately. Although not evident from the figures, diurnal changes in K are small. Unlike the hemispheric curves of Min and Horn (1982) and the regional findings of Koehler and Min (1983) for A, which is strongly influenced by the variability of temperature near the surface, there is no large daily variation in wind that contributes strongly to the vertically integrated K.
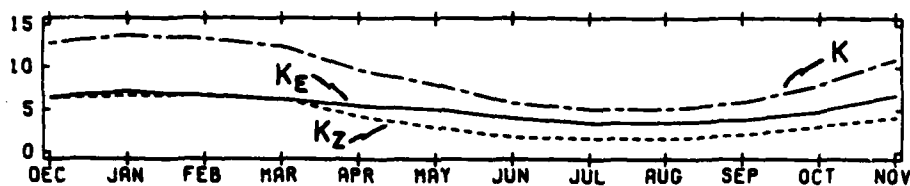
Figure 2. Monthly means of K values shown in Fig. 1. Total (dash-dot), zonal (dash) and eddy (solid). Units: 10^5 Jm^{-2}.
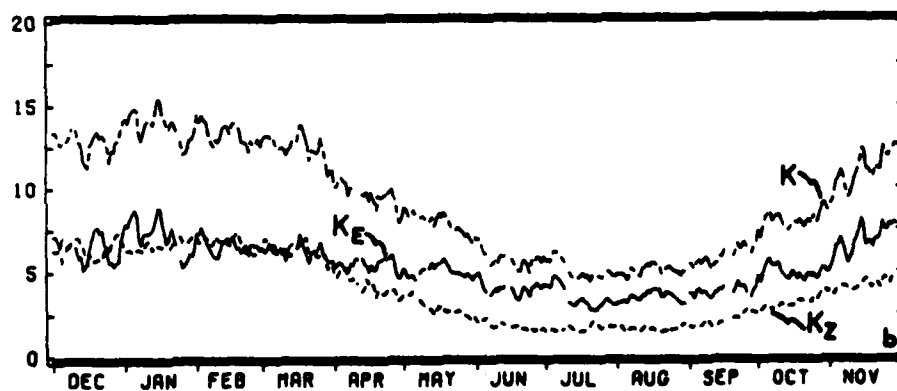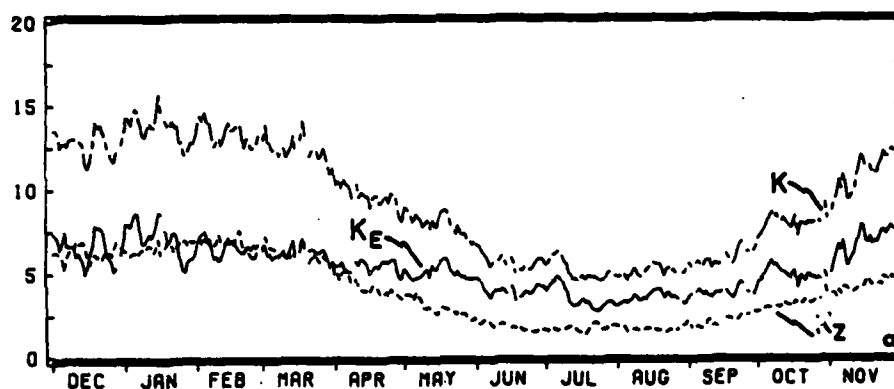

Figure 3. Time series of daily K values from Fig. 1 but for only a) 0000 GMT and b) 1200 GMT. Total (dash-dot), zonal (dash) and eddy (solid). Units 10^5 Jm^{-2}.

b. Standing and transient components of K_E

Special attention is given to K_E since it is the energy of motion in atmospheric disturbances. K_E was partitioned into its standing $(\overline{K}_{Est})$ and transient $(\overline{K}_{Etr})$ components using Equations 4 and 5. Figure 4 shows the monthly values of $\overline{K}_{Est}$ and $\overline{K}_{Etr}$. $\overline{K}_{Est}$ shows only a weak annual cycle and compares favorably with the findings of Peixoto and Oort (1974). The $\overline{K}_{Etr}$ curve is larger than $\overline{K}_{Est}$ throughout the year and exhibits a stronger annual cycle. The $\overline{K}_{Etr}$ values found here are about 27% lower than those of Peixoto and Oort. From examination of Table 2 it is clear that the majority of the monthly differences in total kinetic energy (K) between the studies seems to be accounted for by the differences in $\overline{K}_{Etr}$. The values in Table 2 are in specific units (Jkg^{-1}); for comparison pur- poses Peixoto and Oort (1974) values were converted to specific units. This was done because of the different vertical domains, i.e., 1000-100 mb for Peixoto and Oort and surface to 370K (about
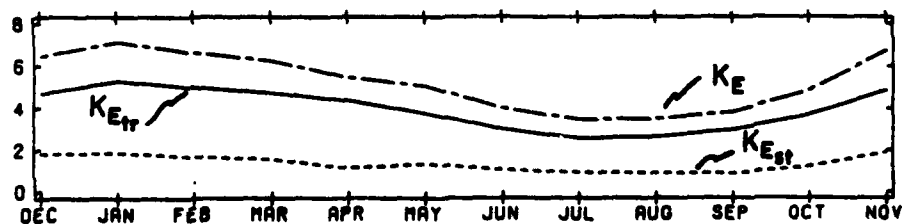

Figure 4. Eddy K (dash-dot) partitioned into standing eddy (dash) and transient eddy (solid). Units 10^5 Jm^{-2}.

Table 2. Monthly mean values of kinetic energy. Results of this
study are compared with the five year average values from
Peixoto and Oort (1974) (converted to specific units).
Units: Jkg^{-1}

Mo.	$\bar{K}$ FGGE	Peixoto & Oort	Mo.	$\bar{K}_z$ FGGE	Peixoto & Oort
D	147.2	167.7	D	72.7	73.7
J	158.2	188.8	J	75.9	84.4
F	153.7	185.1	F	77.6	90.4
M	143.9	166.5	M	72.0	79.7
A	111.2	132.7	A	48.4	54.4
M	91.7	102.4	M	33.4	32.3
J	66.4	84.1	J	20.2	22.2
J	59.0	73.3	J	18.9	20.4
A	58.8	80.3	A	18.4	24.9
S	68.0	91.4	S	23.9	29.4
O	92.2	111.1	O	35.9	37.1
N	126.0	138.0	N	47.9	53.8

Mo.	K_{Etr} FGGE	Peixoto & Oort	Mo.	$\bar{K}_{Est}$ FGGE	Peixoto & Oort
D	53.9	75.0	D	20.5	18.9
J	61.1	78.3	J	21.2	23.1
F	57.3	72.6	F	18.9	22.1
M	54.4	70.8	M	17.5	16.1
A	50.0	67.9	A	12.7	10.5
M	43.2	60.9	M	15.1	9.4
J	34.4	51.1	J	11.8	10.9
J	29.5	44.3	J	10.5	11.7
A	30.4	44.9	A	10.1	10.5
S	34.3	52.2	S	9.8	9.8
O	42.6	62.6	O	13.7	11.3
N	56.2	68.4	N	21.8	15.8

150 mb) here. Although the calculations obtained in this study do
not include contributions from about 150 to 100 mb, $\overline{K}_{Etr}$ still seems
lower than what might be expected from Peixoto and Oort's five year
average data from May 1958 to April 1963. The remaining difference
can in part be explained by comparing calculation methods. Peixoto
and Oort interpolate monthly statistics (such as $\overline{v'^2}$) from stations
to grid points rather than interpolating the basic data (e.g., v)
and then calculating energy quantities as was done here. The re-
sult is that the estimates are different.

To illustrate the calculation differences, assume a square
array of equally spaced data points surrounding a central grid
point. The data points are numbered *clockwise starting* in the
upper left hand corner; the central grid point is zero. As an
example, imagine a sinusoidal wave propagates through this array
in five time periods, a.. through e., where both time periods a.
and e. correspond with the data grid positioned in the light winds
under the ridge. Period c. centers the grid directly on the trough
while time periods b. and d. place the grid at intermediate posi-
tions. With this arrangement, $\overline{v'^2}$ is computed by the two different
methods. The upper portion of Table 3 shows the hypothetical v
components at the four data points and their deviations from the
time average (v') in parentheses. Values for the central grid
point 0·are the result of interpolating at each time period. In
the lower portion of the table, $\overline{v'^2}$ calculated from the interpolated
v' values is 24 m^2s^{-2}. The values to the extreme right are the re-

Table 3. Data and results for comparison of two different interpolation techniques. a) v and v' (in parenthesis) are shown at data points and a central grid point for five time periods. Units: ms^{-1} b) v'^2 calculations for all points. Note discrepancy in the two resulting $\overline{v'^2}$. See text for explanation. Units: m^2s^{-2}.

a)

Position Time	0 v	0 v'	1 v	1 v'	2 v	2 v'	3 v	3 v'	4 v	4 v'
a	-2.5	(-1.5)	0	(2)	-5	(-5)	-5	(-4)	0	(1)
b	7.5	(8.5)	10	(12)	5	(5)	5	(6)	10	(11)
c	0	(1)	-20	(-18)	20	(20)	15	(16)	-15	(-14)
d	-7.5	(-6.5)	-5	(-3)	-10	(-10)	-10	(-9)	-5	(-4)
e	-2.5	(-1.5)	5	(7)	-10	(-10)	-10	(-9)	5	(6)
$\overline{v}$	-1		-2		0		-1		-1	

b)

Position Time	0	1	2	3	4
a	2.25	4	25	16	1
b	72.25	144	25	36	121
c	1	324	400	256	196
d	42.25	9	100	81	16
e	2.25	49	100	81	36
$\overline{v'^2}$	24	106	130	94	74 101

sult of time averaging at each data point and then interpolating. For $\overline{v'^2}$ this value is 101 $m^2 s^{-2}$. As shown by this hypothetical example, the method of interpolation gives large differences for the $\overline{v'^2}$ quantity. The computational method chosen by Peixoto and Oort will produce larger (or equivalent) $\overline{K}_{Etr}$ estimates. $\overline{K}_{Est}$ values are comparable between studies since the interpolation was analogous to that shown in the upper portion of Table 3, where no differences result. In addition, Peixoto and Oort find $\overline{K}_E$ as the sum of $\overline{K}_{Est}$ and $\overline{K}_{Etr}$. Here, $\overline{K}_{Etr}$ is found as a residual of the average of twice daily values of K_E and monthly $\overline{K}_{Est}$ (Eq. 4). Thus, the two methods will give dissimilar values for $\overline{K}_{Etr}$ and $\overline{K}_E$. These differences should be tacitly noted when comparing $\overline{K}_E$ values.

To further understand the behavior of $\overline{K}_{Est}$ and $\overline{K}_{Etr}$, plots showing each as a function of time and latitude were prepared. $\overline{K}_{Est}$ and $\overline{K}_{Etr}$ are presented in Figure 5. The average values for each zonal ring (weighted by the area of the ring) are plotted for each month. The standing component of K_E in Figure 5a exhibits three relative maxima during the year. These regions are marked by heavy dashed lines. The first region is a band of strong $\overline{K}_{Est}$ between 55-60°N present during the winter months. This maximum corresponds closely with the latitude of the east-west monthly mean trough positions. The mean 700 mb height map from Taubensee (1979) reproduced in Figure 6 for December shows a well developed low over northeast Siberia and a trough extending eastward through a southward displaced Icelandic low to just west of Ireland. The east-west
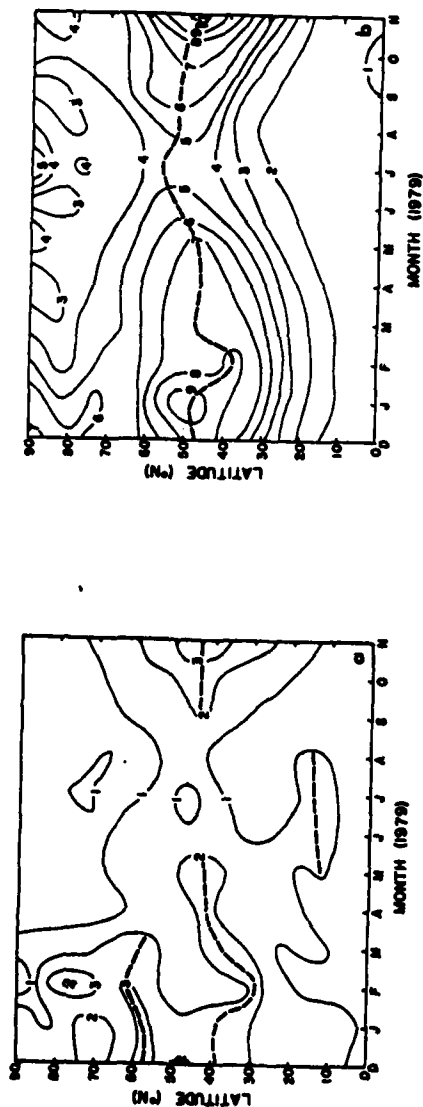
Figure 5. a) Standing eddy K and b) transient eddy K as a function of month and latitude. Heavy dashed lines are drawn through zones of relative maximum values. Units: 10^5 Jm^{-2}.

axis of these features is roughly along 55°N. These features contri-

bute to K_E by large deviations in both u and v. The high latitude

maximum persists through January, February and March and exhibits

behavior consistent with December. The maximum between 70 and 80°N

which appears in February overshadows the relative maximum near 60°N.

An examination of the mean 700 mb map from Dickson (1979), repro-

duced in Figure 7, shows a strong omega block over the Bering

Strait and a wave number 2 pattern with intense upper level lows

over north central Asia and the Canadian archipelago. These features

contribute very strong departure values. Inspection of daily 500 and

300 mb maps from the European Centre for Medium Range Forecasts

(Bjorheim et al., 1981) also reveal patterns that would contribute
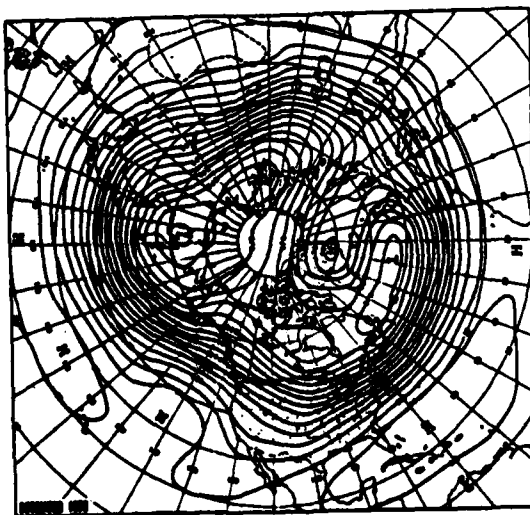

Figure 6. Mean 700 mb height contours (dam) for December 1978 from
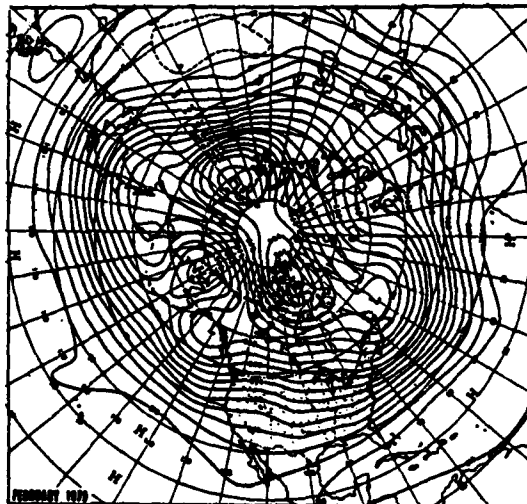   Taubensee (1979).

Figure 7. Mean 700 mb height contours (dam) for February 1979
         from Dickson (1979).

to a large standing eddy component. From this comparison it seems

plausible that strong and persistent high latitude trough and ridge

positions are delineated by large values of $\bar{K}_{Est}$, particularly when

they occur in essentially the same zonal ring.

The second region of large $\bar{K}_{Est}$ can be followed through nearly

the entire FGGE year. Its seasonal cycle very closely follows the

latitude bands of the axis of the mean jet stream position. This

agrees favorably with the position of maximum zonally averaged

monthly geostrophic winds computed from the pressure level height

information from Crutcher and Meserve (1970). This maximum will be

further discussed below. It should be noted that no double maximum

appears in November as had been present in the previous December.

Inspection of the 700 mb flow pattern presented by Dickson (1980)

does not show as broad or as strong 700 mb features as were present
early in the FGGE year.

The third region of relatively high values of $\overline{K}_{Est}$ occurs in
summer at about 15°N. This feature is probably associated with the
land-ocean heating contrasts which generate the summer monsoon.
Some evidence that this is a monsoon signal will be given in the
next section.

The time-latitude plot of transient K_E shown in Figure 5b ex-
hibits only one relative maximum during the year. The heavy dashed
line drawn through the figure appears similar to the second maximum
discussed for $\overline{K}_{Est}$, but is more clearly defined. It tends to be
located about 5 to 10° north of the $\overline{K}_{Est}$ maximum for each month
throughout the year. As a possible explanation of this displace-
ment one might imagine a transient eddy (e.g., a cyclone) forming
near the axis of the $\overline{K}_{Est}$ maxima (near a jet stream maxima). As
the storm matures it moves to the northeast and intensifies. This
process of an eddy moving northeast and intensifying would tend to
move the maximum $\overline{K}_{Etr}$ contribution to a more northerly latitude band.
A comparison of $\overline{K}_{Etr}$ with the latitudes of FGGE year cyclogenesis
prepared by L. Whittaker, and shown in Figure 8, lends support to
this view. Comparison of Figures 5b and 8, in general, shows that
the maximum values of $\overline{K}_{Etr}$ appear 5 to 10° north of the average
latitude of greatest cyclogenetic activity as determined from the
12 cyclone contour. Noteable exceptions occur in February and May
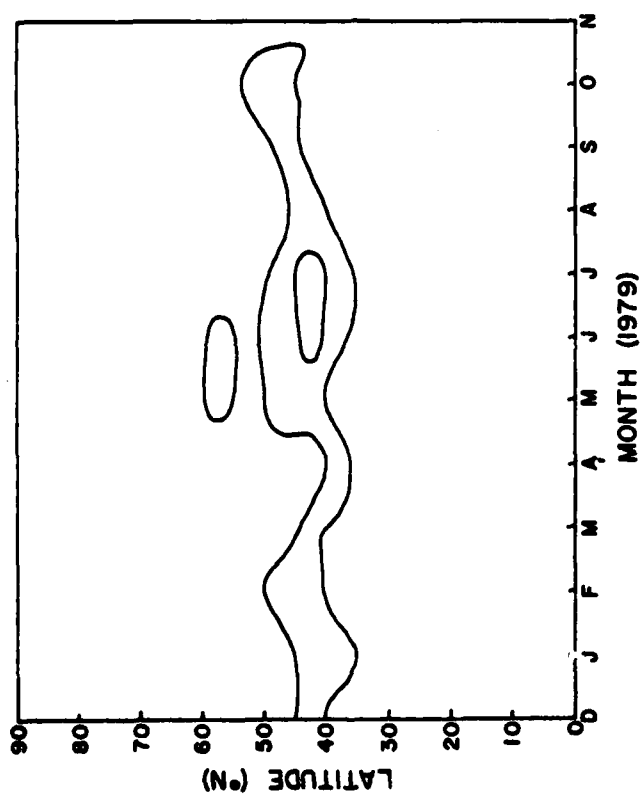when the maximum cyclogenesis count in one latitude ring occurs north

Figure 8. FGGE year cyclogenesis for each 5° zonal ring. Isopleth encloses 12 and greater cyclone events.

MONTH (1979)

LATITUDE (°N)

of the $\overline{K}_{Etr}$ maximum. Comparison of FGGE cyclogenesis with that
found by Olson (1982) for the period 1958-1977 shows cyclogenesis
during February and May of the FGGE year to be displaced about 10°
north of the long term mean. These two months seem to contradict
the idea that $\overline{K}_{Etr}$ should appear north of the cyclone maximum, how-
ever, it should be noted that cyclone intensity is not represented
in Figure 8. It is possible that a lesser number of long lived,
intense cyclones in a lower latitude belt could contribute to larger
$\overline{K}_{Etr}$ than frequent, short lived, weak cyclones in a higher latitude
belt. An examination of the cyclones that formed in high latitudes
during February and May revealed the storms were generally shorter
lived and less intense than those further south (L. Whittaker,
1983). In addition, no mention has been made regarding how anti-
cyclones contribute to $\overline{K}_{Etr}$.

Min and Horn (1982) showed that transient eddy A ($\overline{A}_{Etr}$) in
the exact form for the FGGE year corresponded quite closely to the
zones of maximum cyclogenesis found by Whittaker and Horn (1981)
for North America and Whittaker and Horn (1982) and Klein (1957)
for the Northern Hemisphere. It is interesting to compare $\overline{K}_{Etr}$ with
transient eddy A from their study. Figure 9 shows the transient
eddy A from Min and Horn (1982) for the exact and variable approxi-
mate formulations of A. Comparing Figure 9a with Figure 5b reveals
the similar shape of the maxima of both plots. The $\overline{K}_{Etr}$ maxima
appears at or slightly north (within one 5° latitude ring on average)
of the exact $\overline{A}_{Etr}$ maximum. If cyclogenesis is closely associated
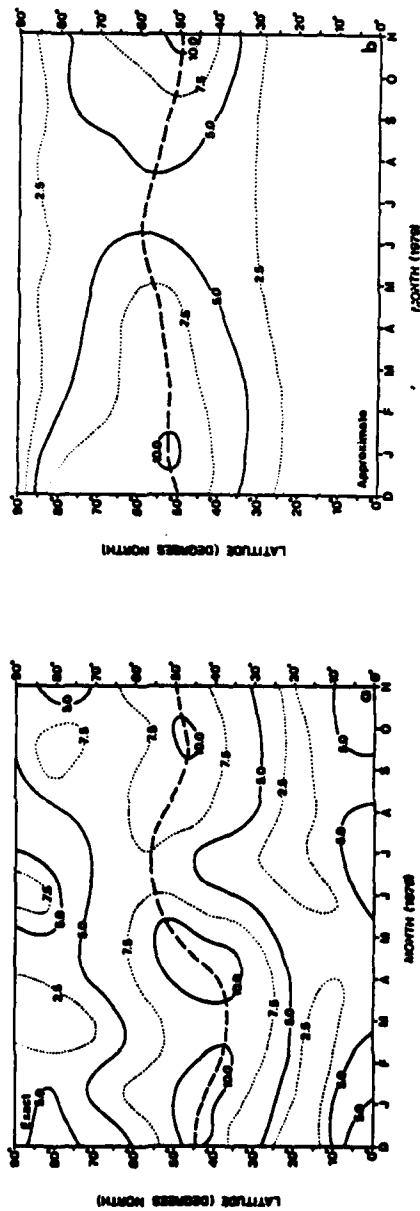
Figure 9. Transient eddy A as a function of month and latitude. Heavy dashed lines through zones of maximum values. a) Exact form. b) Variable approximate form. Units: 105 Jm−2 (Adapted from Min and Horn (1982).)

with the $\overline{A}_{Etr}$ maximum, then once formed, the cyclones intensify and, generally, move to the northeast. Thus, they displace the $\overline{K}_{Etr}$ maximum northward. In contrast, comparison of the approximate $\overline{A}_{Etr}$ maximum (Fig. 9b) with the $\overline{K}_{Etr}$ maximum shows a poor fit. In fact, $\overline{K}_{Etr}$ averages 5 to 10° south of the $\overline{A}_{Etr}$ maximum. This seems to further support the argument of Min and Horn (1982) that the exact formulation of A should be used for studying cyclone activity.

c. Geographic distribution of K, K_E and their standard deviations

In this section the geographical distributions of K and K_E are presented along with their standard deviations. The values are ex-pressed in specific units (Jkg^{-1}) because the vertical integration does not contain the same amount of mass in every grid square. Dis-tributions from Lahey et al. (1960) of 300 mb geostrophic K are referenced in this section to provide a rough estimate of differences in the FGGE year distributions from a multi-year average. Because the integrated values of K versus geostrophic K at one level are not entirely comparable, only very general comparisons are possible. However, it should be noted that 300 mb is near the level of maximum K contribution. Mid-season months from Lahey et al. (1960) were chosen for comparison with seasonal maps produced here.

Figure 10a shows K for grid squares and cyclone tracks for the FGGE winter (DJF). Two strong centers of K appear, one off the east coast of Asia and an equally strong one just north of Cape Hatteras
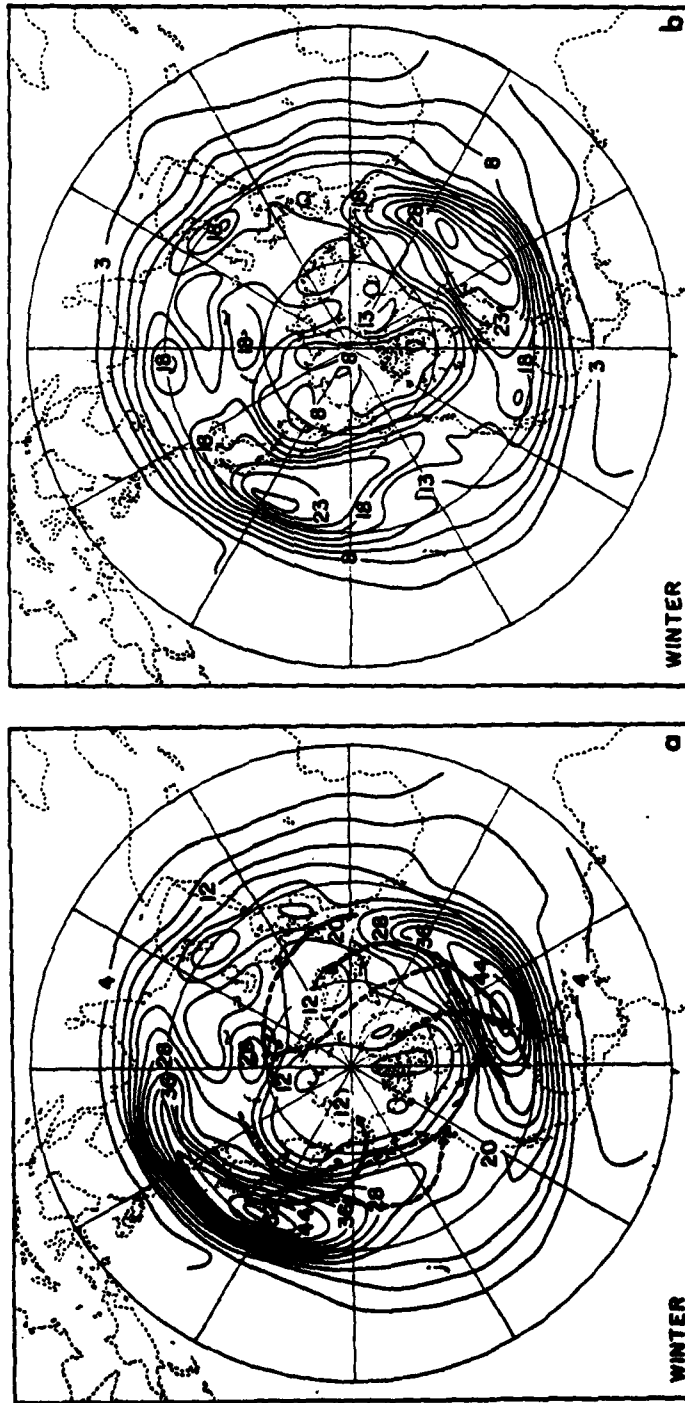
Figure 10. a) Distribution of total K based on grid point values for the FGGE winter (DJF) with primary cyclone tracks (solid) and secondary cyclone tracks (dashed). b) Standard deviation of K. Units: 10 Jkg^{-1}.

on the U.S. coast. A third, weaker maximum appears over the Arabian

peninsula. These are generated, primarily, by the strong upper

level jet streams in these regions of strong thermal land/ocean

contrast. The position of the centers are in general agreement with

Lahey et al. (1960), however, the two FGGE east coast maxima are

nearly the same intensity while the long term average shows the

Asian maximum to be much stronger than the North American maximum.

Extremely cold weather over the North American continent during the

FGGE winter probably led to larger baroclinicity which supported

stronger winds and gave the larger K maximum. Standard devia-

tions of K in Figure 10b look similar to the map of K. The figure

seems to reflect the pulsing and east-west elongation of the wind

through its average position.

In Figure 10a, cyclone tracks from the FGGE winter agree quite

well with observations of cyclone activity in relation to upper

level winds. Since K is vertically integrated, and the largest

contributions occur from the layers near wind maxima, one can think

of the K map roughly representing mean jet stream positions. The

superimposed cyclone tracks, in general, show cyclogenesis near the

axis of a K maxima. As the storms mature, they move away to the

north and east, and decay at a higher latitude.

Figure 11a which displays the K_E distribution for the FGGE

winter, illustrates that care should be taken in interpretation of

the results presented here. Note the large eddy values off the

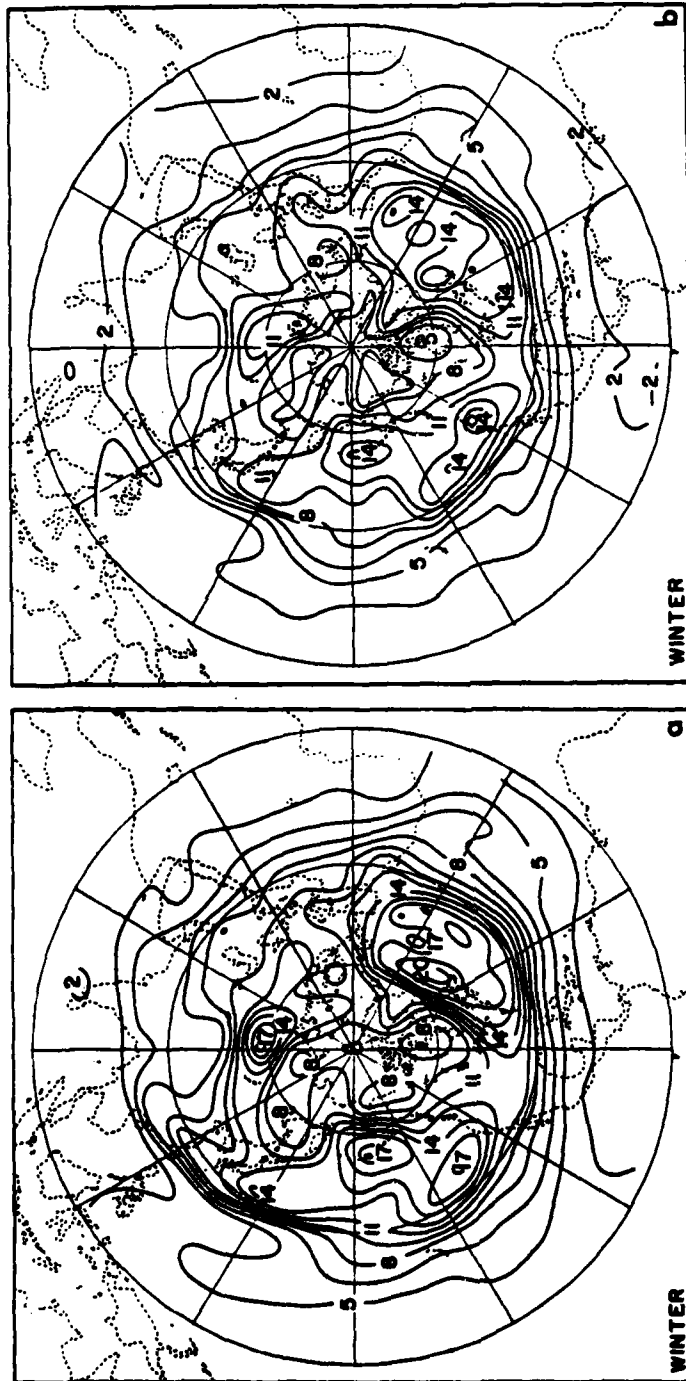California coast. Recall that eddy values represent departures

Figure 11. a) Distribution of eddy K based on grid point values for the FGGE winter (DJF).
b) Standard deviation of K_E. Units: 10 Jkg^{-1}.

from the zonal mean. Thus, for example, if the observed u component was small in an area while $\bar{u}$ is large for the zonal ring, the resulting u' (=u-$\bar{u}$) is large negative which becomes very large positive when squared. In a sense, such a region is an example of, for lack of a better name, a K_E "hole." Large standard deviations of K_E (Fig. 11b) appear in this region as well. A review of mean 700 mb maps show ridging in December and January with troughing in February over this area. (See Figs. 6 and 7 and Wagner (1979).) This variation in troughs and ridges produces the large standard deviations in this region for the winter season. This example off the California coast points to the importance of interpreting K_E plots only after considering other features in the zonal ring, inspecting K plots, and reviewing flow patterns which generate the energy fields.

Changes from winter to spring (MAM) are most evident in spring K shown in Figure 12. The Asian maximum has been displaced east and slightly north of its winter position and has weakened slightly. It, and the Mediterranean/Arabian maximum appear consistent with the 300 mb K patterns of Lahey et al. (1960). On the east coast of North America, however, the winter maximum nearly disappears. Figure 1 in Koehler and Min (1983) shows that the strong gradient of A present in winter all but disappears from the North American coast in spring. The baroclinicity is greatly weakened and cannot support strong winds aloft. In addition, cyclogenesis off the U.S. east coast is lower for the FGGE spring than the long term
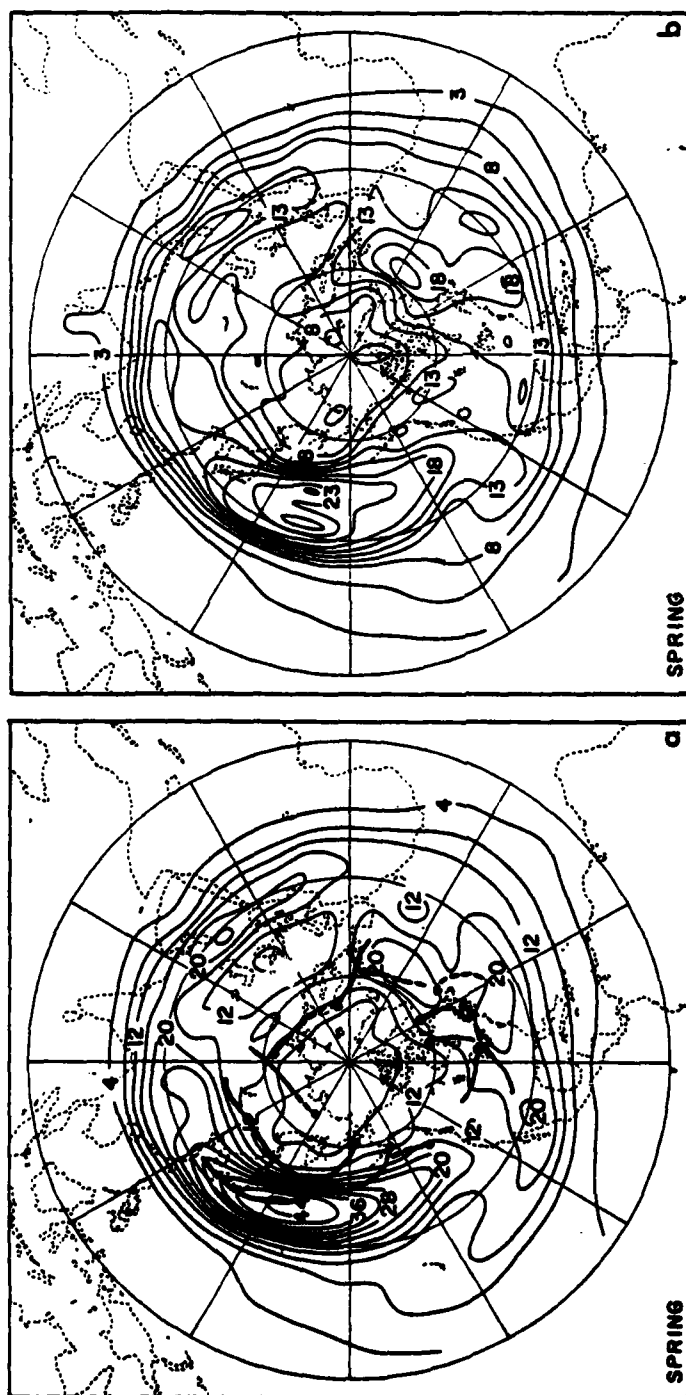
35

SPRING

SPRING

Figure 12. Same as Fig. 10, except for spring (MAM).

average as presented by Whittaker and Horn (1981). These three
things seem self consistent in that weak baroclinicity and weak winds
provide less favorable conditions for cyclogenesis. As with Figure
11, Figure 13 presents K_E and its standard deviation.

Summer (JJA) finds the continental east coast maxima displaced
to their most northerly positions and at their weakest intensity,
as shown in Figure 14. Perhaps the most striking feature of summer
is the signature of the Indian monsoon. Its signature is present
in all summer maps. K shows an isolated center of greater than
40 Jkg^{-1} over the Indian subcontinent that is not present in any
other season. A standard deviation in K of greater than 30 Jkg^{-1}
extends over the same region. The greater than 50 Jkg^{-1} contour of
K_E shown in Figure 15a reflects the Indian monsoon. Both the
standard deviation of K (Fig. 14b) and of K_E (Fig. 15b) reflects
the time change in the monsoon. The relatively large deviations re-
flect an intensifying of the circulation in early summer followed
by a weakening in late summer. The most likely features responsible
for the large values are the low level Somali jet and the high level
Easterly Jet which extends from the Indian subcontinent westward
into Africa. As mentioned earlier in relation to the time-latitude
variation of K_E, these features contribute to a low latitude summer
standing eddy maximum in the latitude bands of the Indian subcontin-
ent (See Fig. 5a).

Autumn (SON) brings an increase in K with strong maxima return-
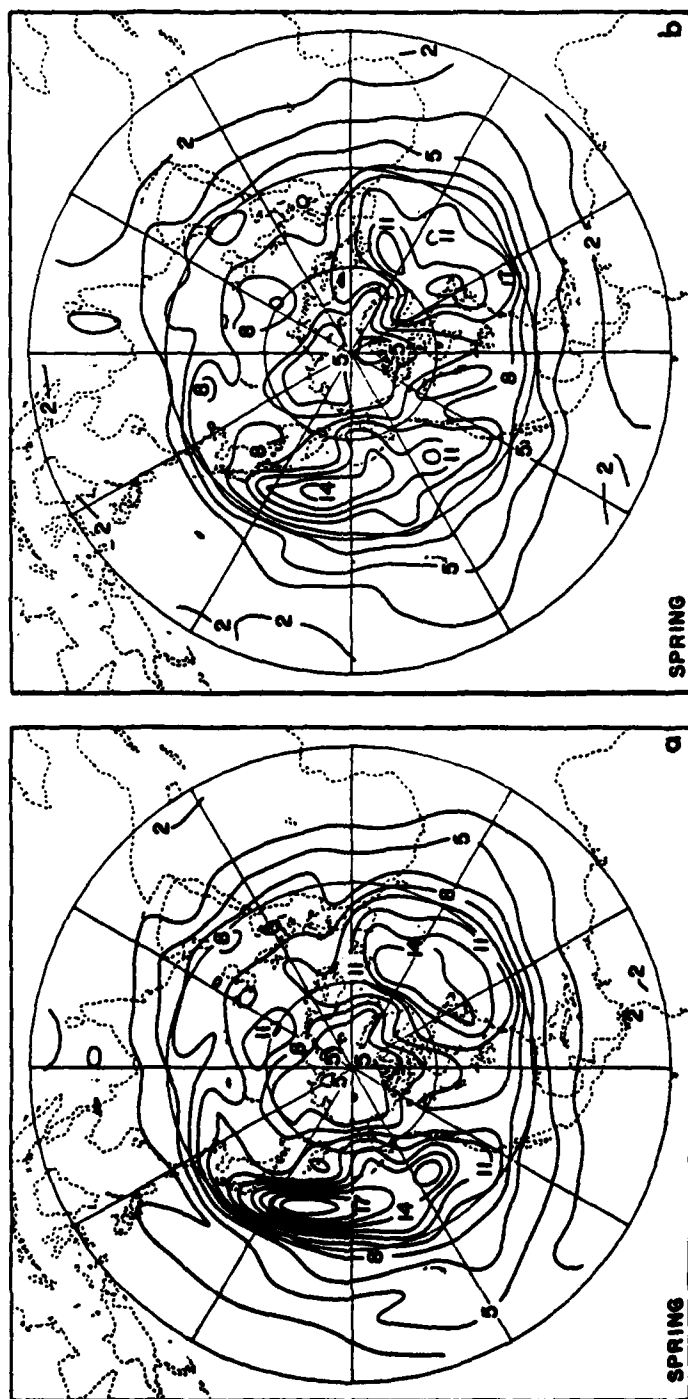ing to the North Pacific and North America off the east coast of the

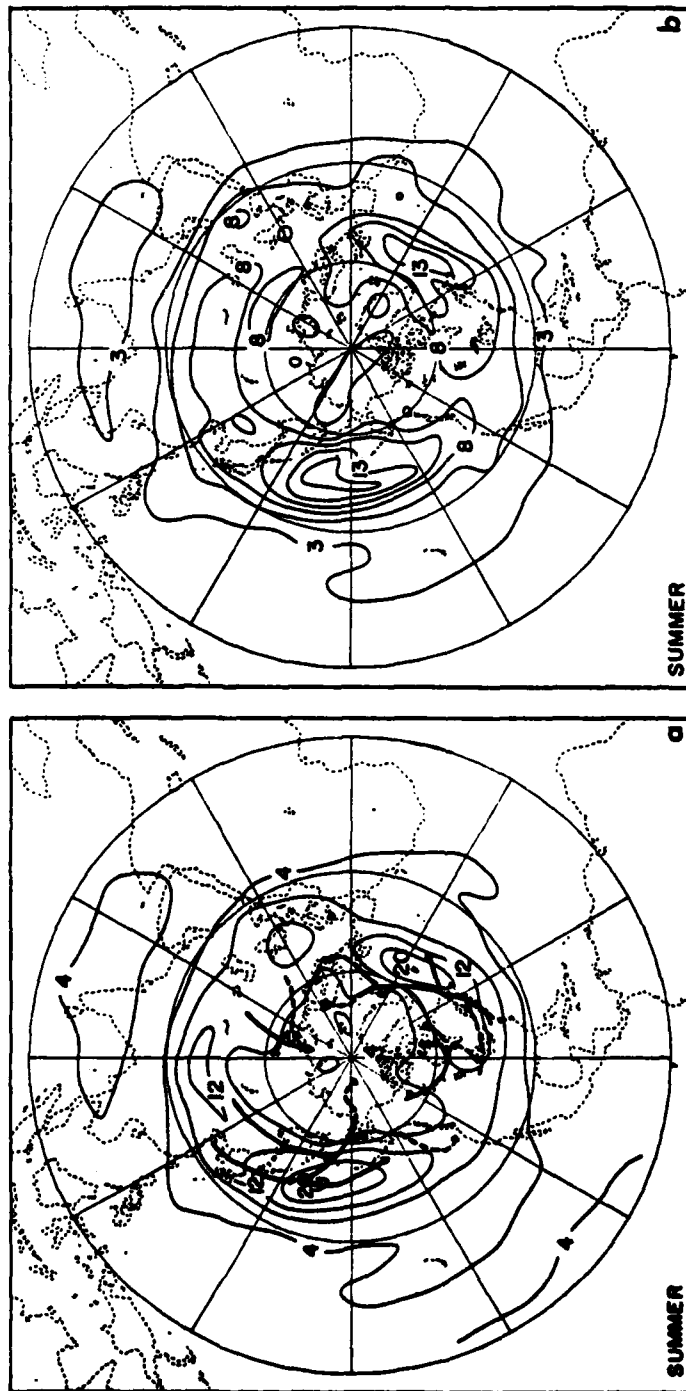Figure 13. Same as Fig. 11, except for spring (MAM).

38

SUMMER

SUMMER

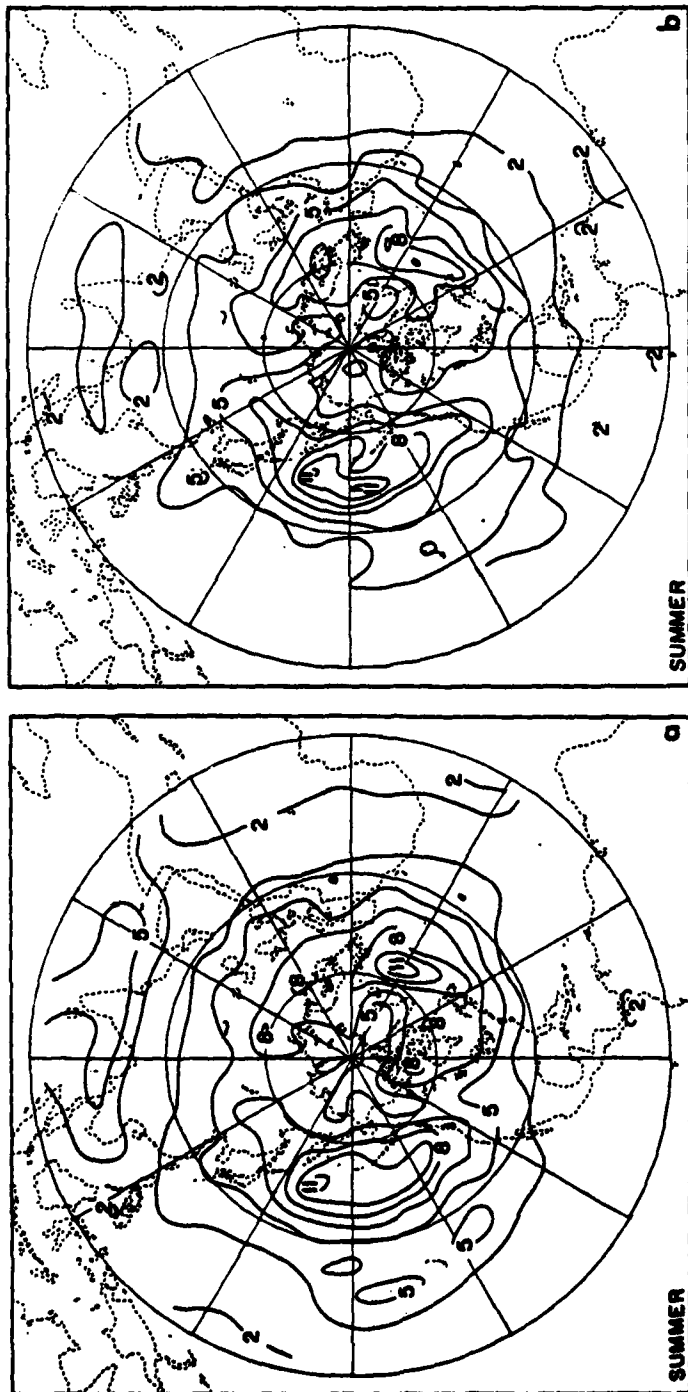Figure 14. Same as Fig. 10, except for summer (JJA).

Figure 15. Same as Fig. 11, except for summer (JJA).

continents. The centers are still displaced north of their mean

winter positions, however. Figures 16 and 17 show the plots of K,

K_E and their standard deviations.

This section has shown some of the differences in the geographi-

cal distribution of kinetic energy in the FGGE year. Noteworthy

features include the nearly equally strong Asian and North American

K maxima in winter and a near total collapse of the North American

maxima in spring. This weaker maxima is reflected in reduced baro-

clinicity in exact A plots from Koehler and Min (1983) and in re-

duced cyclogenesis in the region. The most striking feature of

summer is the strong signal of the Indian monsoon.

d. Ratios of kinetic to available potential energy

The A calculations of Min and Horn (1982) and those for K per-

formed here allow ratios of various quantities to be formed, as was

done by Peixoto and Oort (1974). Table 4 contains monthly A from

Min and Horn (1982) for the approximate and exact A formulations and

the approximate A from the five years of data calculations performed

by Peixoto and Oort (1974). Peixoto and Oort's values have been

converted to specific units for comparison. Table 2, presented

earlier, contains the K quantities, and Table 5 contains the ratios

of K and A as calculated from the values in Tables 2 and 4.

Many of the differences between the quantities of available

potential energy presented in Table 4 have been discussed in Min

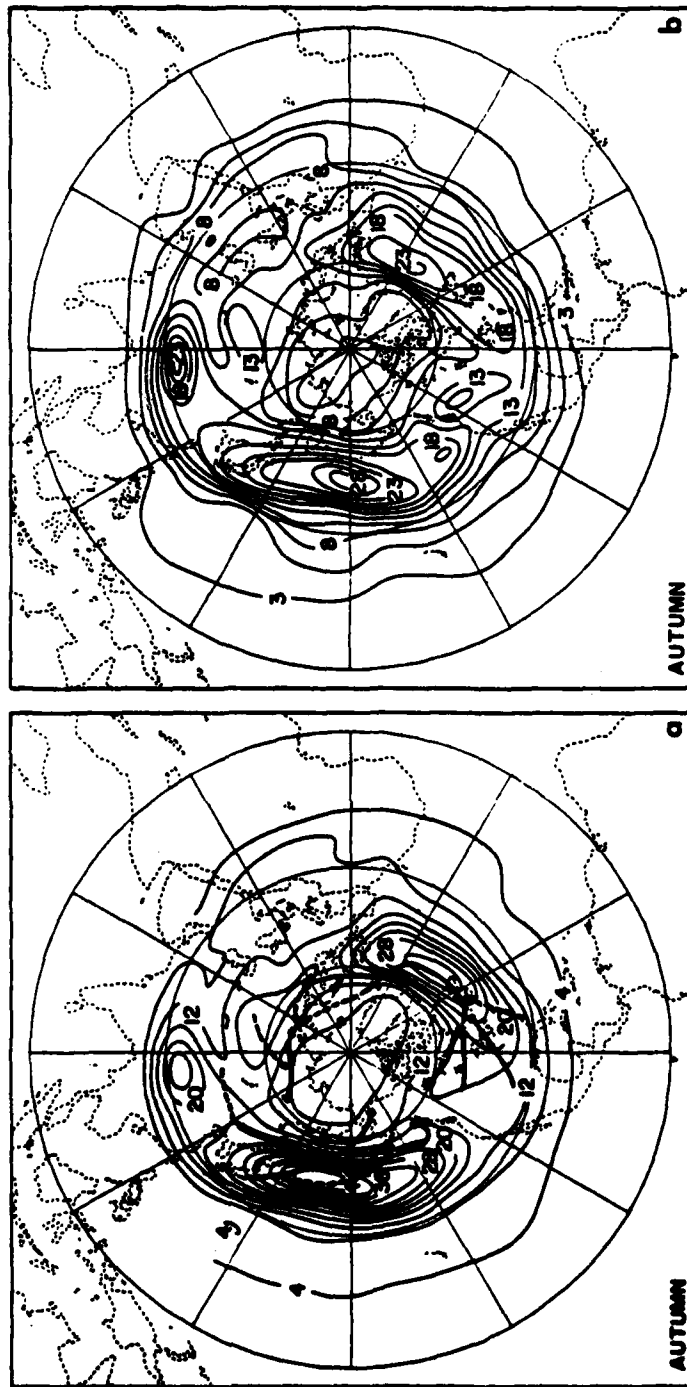and Horn (1982) and Min (1981), however, some items should be re-

41

AUTUMN

b

AUTUMN

a

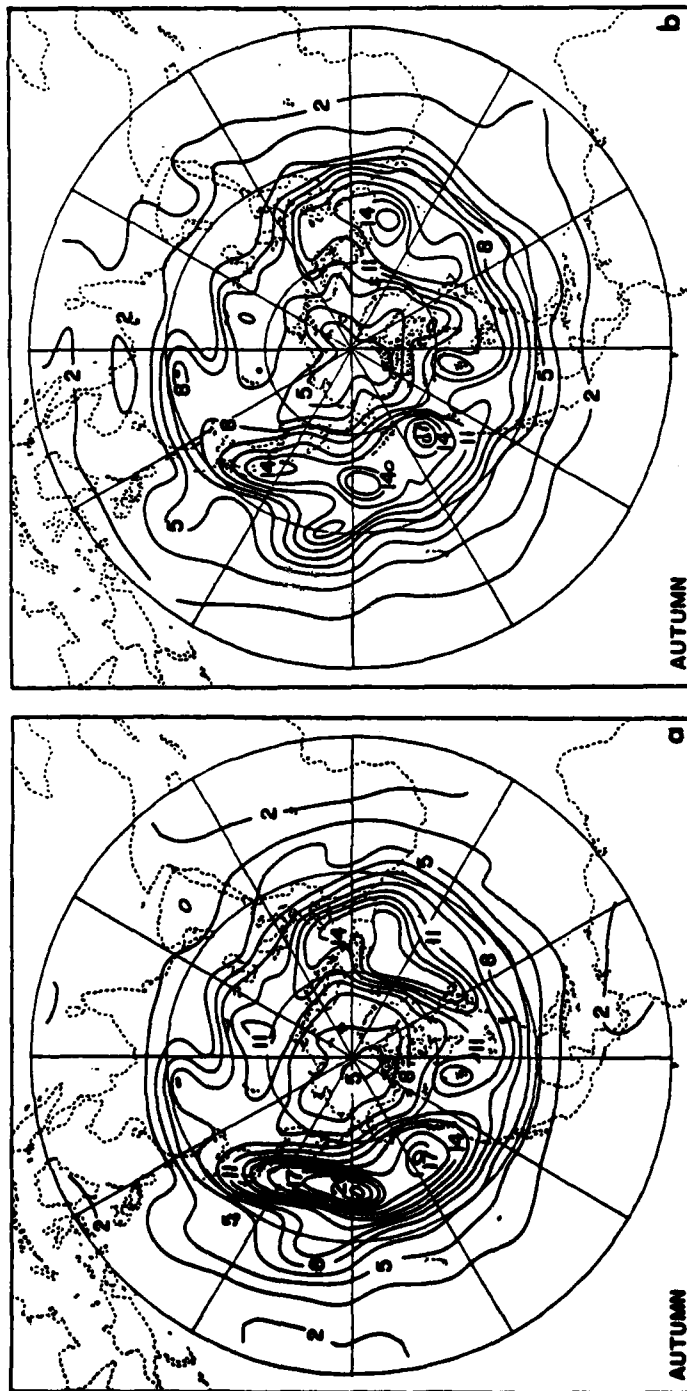Figure 16. Same as Fig. 10, except for autumn (SON).

42

Figure 17. Same as Fig. 11, except for autumn (SON).

Table 4.   Monthly mean values of available potential energy.   Left
two columns are exact and approximate A from Min (1981)
and third column is approximate A from Peixoto and
Oort (1974) (converted to specific units). Units: Jkg^{-1}

	$\overline{A}$				$\overline{A_z}$	
Mo.	Exact	Approx.	Peixoto & Oort	Mo.	Exact	Approx.	Peixoto & Oort
D	579.9	660.1	686.0	D	371.6	568.2	584.7
J	607.4	710.0	721.9	J	392.0	605.8	607.6
F	580.5	722.1	717.6	F	380.9	633.1	614.1
M	552.9	643.5	674.0	M	338.1	567.5	584.7
A	510.4	571.5	536.8	A	275.8	499.3	461.7
M	425.2	421.7	400.7	M	185.6	357.2	329.9
J	323.6	282.2	269.0	J	82.2	219.6	204.7
J	266.6	203.8	202.5	J	33.3	147.1	141.6
A	306.2	233.8	218.9	A	74.7	179.0	163.3
S	360.7	319.7	320.1	S	161.8	271.0	259.2
O	429.9	460.8	457.3	O	250.6	401.5	381.1
N	507.1	588.7	597.8	N	306.6	503.9	504.2

	$\overline{A}_{Etr}$				$\overline{A}_{Est}$	
Mo.	Exact	Approx.	Peixoto & Oort	Mo.	Exact	Approx.	Peixoto & Oort
D	64.7	50.0	60.3	D	139.6	41.9	41.1
J	73.3	55.6	63.7	J	142.1	48.6	50.5
F	64.0	49.4	59.8	F	135.6	39.6	43.3
M	54.6	45.3	56.2	M	160.1	30.7	32.7
A	71.8	48.4	52.3	A	162.9	23.8	18.1
M	70.4	39.9	51.7	M	169.3	24.6	18.9
J	56.0	32.1	44.1	J	185.4	30.5	20.5
J	49.6	27.1	37.5	J	183.7	29.6	23.7
A	56.2	29.0	36.9	A	175.3	25.8	18.7
S	64.2	30.1	46.3	S	134.7	18.6	14.5
O	67.7	38.6	54.0	O	111.7	20.7	21.6
N	70.5	48.6	58.6	N	130.0	36.2	35.5

Table 5. Ratios of mean monthly kinetic energy and available
potential energy quantities. The left hand column pre-
sents ratios based on exact A, while the two right columns
show values based on the approximate A as calculated by
Min (1981) for the FGGE year and Peixoto and Oort (1974)
for a five year period. For K_E to K_Z ratios, the left
column is for the FGGE year and the right column is the
five year average from Peixoto and Oort.

	$\overline{K}/\overline{A}$				$\overline{K}_E/\overline{K}_Z$	
Mo.	Exact	Approx.	Peixoto and Oort	Mo.	FGGE	Peixoto & Oort
D	.26	.22	.24	D	1.02	1.27
J	.26	.22	.26	J	1.08	1.16
F	.27	.21	.26	F	.98	1.05
M	.26	.22	.25	M	1.00	1.09
A	.22	.19	.25	A	1.30	1.44
M	.22	.22	.26	M	1.75	2.18
J	.21	.24	.31	J	2.29	2.78
J	.22	.29	.38	J	2.12	2.75
A	.19	.25	.37	A	2.20	2.22
S	.19	.21	.29	S	1.85	2.11
O	.22	.20	.24	O	1.57	1.99
N	.25	.21	.23	N	1.63	1.56

	$\overline{A}_E/\overline{A}_Z$		
Mo.	Exact	Approx.	Peixoto & Oort
D	.55	.16	.17
J	.55	.17	.19
F	.52	.14	.17
M	.64	.13	.15
A	.85	.14	.16
M	1.30	.18	.21
J	2.96	.29	.32
J	7.11	.39	.43
A	3.08	.31	.34
S	1.22	.18	.23
O	.72	.15	.23
N	.65	.17	.19

emphasized since they are important in explaining the differences in ratios shown in Table 5 and discussed below. Very large differences occur in the partitioning of A into zonal and eddy components depending on whether the exact or approximate formulation is used. Although the annual cycle of total A and A_Z in the approximate form is slightly larger than in the exact form, A_E in the exact form is nearly twice as large throughout the year, and exhibits a slight summer maximum rather than a minimum as found for the approximate form. A_E is larger than A_Z during the summer months while it is always smaller in the approximate form. The partitioning of A_E into standing and transient components produces quite large differences between the approximate and exact forms. $\overline{A}_{Est}$ is several times larger in the exact form for all months. Note also that while Min (1981) and Peixoto and Oort (1974) agree quite well for approximate A, A_Z and $\overline{A}_{Est}$, approximate $\overline{A}_{Etr}$ from Table 4 is consistently lower by about 20%. This difference is probably attributable to the problem of interpolating data used in obtaining A to grid points rather than interpolating the basic data. This problem was illustrated in an earlier section in relation to wind. Here, the differences arise from $\overline{T'^2}$ quantities in A_E (see equations for A in Min and Horn (1982)) where T' is the time average deviation from the zonal average temperature on an isobaric surface.

Comparing the monthly ratios of K to A in Table 5 from Peixoto and Oort (1974) with those using approximate A determined here, one notes the seasonal trend is similar, however, the ratios from this

study are smaller. This could be due to the different vertical do-
mains of the calculations, different data sets and possibly the
interpolation techniques. The highest ratios of K to A in both
studies occur in summer with somewhat lower ratios in winter. The
ratio of K to A using A in the exact form shows a reversal in the
size of the ratios from winter to summer, with larger ratios in
winter and smaller in summer.

The ratios of K_E to K_Z found here are in general agreement
with those of Peixoto and Oort (1974). Except for November, all
ratios found here are lower. Again, this is probably due primarily
to interpolation differences in computing $\bar{K}_{Etr}$ and the data sets
involved.

5. SPECTRAL ANALYSIS RESULTS

Although the focus of this thesis has been on the temporal and spacial distribution of kinetic energy during the FGGE year, the daily values calculated here readily lend themselves to time series analysis. This brief chapter shows the time series analyses of K, A (both exact and approximate) and their cross spectra. The procedures employed to perform this analysis were discussed in Chapter 3; details of data preparation prior to using an FFT to determine coefficients for the spectral estimates are in Appendix B. Before presenting the time series results, some additional description of the procedure employed is in order.

The spectral estimates presented below were averaged over frequency as suggested by Bendat and Piersol (1971) to increase the number of degrees of freedom (df). Because a 10% cosine taper was applied to each end of the data series, each spectral estimate has only 1.74 df rather than the normal 2 df. Three frequency bins were chosen to form each spectral estimate, allowing 5.22 df. A Markov red noise spectrum was calculated for each series using the method discussed by Mitchell et al. (1966). Note that this may not represent the actual significance since the population to test from is not known. Nevertheless, this provides a background spectrum for comparison. To be consistent with the spectral estimates, three red noise bins were averaged prior to multiplying by the appropriate (chi-squared) χ^2/df value for each confidence limit obtained. For

coherence significance levels of 1% and 5%, the three bin estimates give values of .815 and .713 respectively. See Panofsky and Brier (1958) for this equation.

The resulting power spectra for K, K_Z and K_E are shown in Figure 18. The solid line connects the three frequency bin estimates. The dashed lines are the Markov red noise confidence limits for 90%, 99% and 99.9%. The spectrum is presented as percent variance explained by each frequency band. All three spectra show a number of significant frequencies, however, those at 23 and 26 cycles/year are especially striking. For K (Fig. 18a) the 26 cycles/year frequency exceeds the 99.9% limit and for K_E (Fig. 18c), both 23 and 26 cycles/year are well above the 99.9% confidence limit. They correspond to cycles of about 16 and 14 days respectively. Recall that the visual inspection of Figure 1 suggested that cycles with these periods were prominent in winter and late autumn. They also correspond to the periodic variation found by Miller (1974) during the period January 1964 to May 1966. The results shown in Figure 18c indicate that those cycles appear even when the entire year is examined. The higher significant peak at 26 cycles/year and also one at 32 cycles/year (near 11.5 days) occur in K_E while these frequencies in the K_Z series are not significant. Despite this, cross spectral analysis between K_Z and K_E shows a coherence significant at or above 1% for these frequencies as shown in Figure 19. (The dashed lines are the 1% and 5% significance levels.) Phase angle difference ($\Delta\beta$), not shown, indicates that at
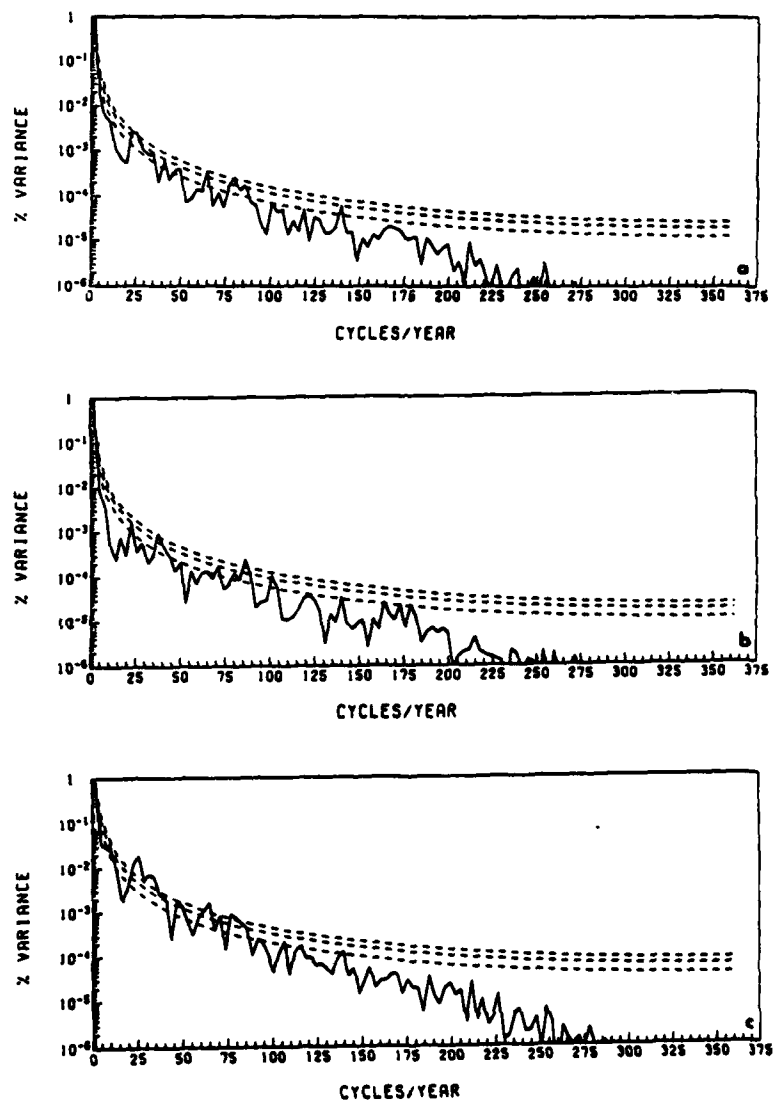
Figure 18. Power variance spectrum for K. Expressed as percent
variance explained. Dashed lines are confidence
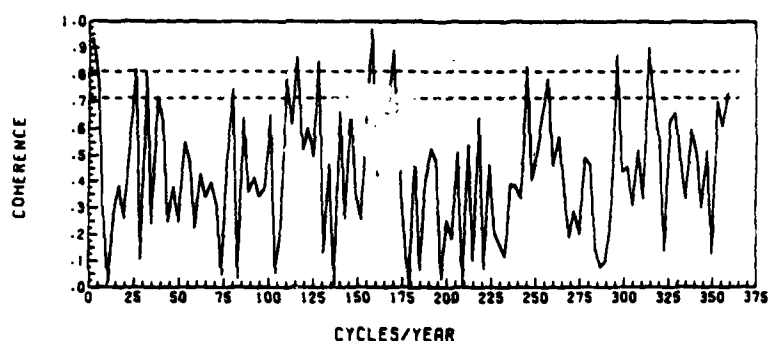limits of 90, 99 and 99.9%. a) K. b) K_Z. c) K_E.

Figure 19. Coherence from cross spectral analysis of K_Z and K_E. Dashed lines are 5% and 1% significance levels.

the 14 day cycle K_E leads K_Z by 135° (5.25 days) and at 11.5 days K_E leads K_Z by 152° (4.86 days). This agrees with our understanding of the energy cycle which shows the flow of energy from K_E to K_Z.

McGuirk and Reiter (1976) noted strong periodicities at about 24 days in several energy quantities from a time series covering nearly ten consecutive years. They noted the periodicity was strongest in the winter months and tended to disappear in summer. With regard to their findings, the FGGE year would appear to be anomolous. No strong periodicity around 24 days was found. The coarseness of resolution at lower frequencies and possible time series errors introduced by interpolating for missing values may have contributed to not observing their cycle. Another explanation could be that the FGGE year was quite different from other years with regard to this particular periodicity.

Because daily A values were available for the period of this study, these time series were also analyzed. Spectral variance estimates were prepared for exact and approximate A and are presented in Appendix C. Coherence estimates between the two A forms and K quantities are also included. The plots are presented with interpretation left to the reader.

6. CONCLUSIONS

Because kinetic energy is so directly related to atmospheric motion, its seasonal and geographical distribution is of particular interest to the meteorologist. This study has focused on twice daily kinetic energy calculated for the Northern Hemisphere using the level IIIa FGGE year (December, 1978-November, 1979) data set. Computations were performed in isentropic (θ) coordinates. Total kinetic energy (K) was divided into its zonal (K_Z) and eddy (K_E) parts, and the results presented as a time series of twice daily values. K_E was further divided into its standing and transient components. The geographical distribution of vertically integrated grid point values of K and K_E were calculated along with their standard deviations. By using exact and approximate available potential energy (A) values from Min and Horn (1982), ratios of K to A were evaluated. Finally, time series of K and A were subjected to spectral and cross spectral analysis. The following major results were obtained:

(1) As expected, time series of twice daily values show quite strong annual cycles. K_E shows the weakest annual cycle. K_Z exhibits a more pronounced annual cycle. Visual inspection reveals that during winter and again in late autumn a strong pulsing occurs at a period of 12 to 16 days.

(2) Comparison of transient eddy K with values from Peixoto and Oort (1974) showed the FGGE values to be lower by about 27%. While

53

year to year differences exist, a smaller vertical domain and systematically lower estimates resulting from a different interpolation method probably are the main contributors to the lower values.

(3) The plot of standing eddy K as a function of time and latitude exhibited three relative maxima during the year. The first was a high latitude maximum associated with persistent east-west trough and ridge features. An extreme case was observed in the 5° latitude bands between 70-80° N during February. It resulted from a very strong, persistent wave number two pattern. The second maximum was present throughout the FGGE year and was closely aligned with the mean monthly jet stream position. The third maximum occurred in summer at about 15°N. This feature appeared to be a monsoon signal.

(4) The time and latitude plot of transient eddy K appeared about 5 to 10° north of the second standing K_E maximum, and in general, the latitude of greatest cyclogenetic activity. Noteable exceptions occurred during February and May when the maximum frequency of cyclogenesis was displaced north of the transient K_E maximum. A comparison of transient K_E with transient eddy available potential energy from Min and Horn (1982) showed the transient K_E maximum north of the exact transient A_E maximum while it was south for approximate transient A_E.

(5) Geographical plots of grid point K showed the Asian and North American east coast maxima to be nearly equal strength during

the FGGE winter (DJF), while the long term mean indicates the Asian

maximum is the stronger. As expected, the upper level maxima are

closely associated with regions of cyclogenesis in winter as well

as the other seasons. A very dramatic change occurred during spring

(MAM): the North American maximum nearly disappears. A weak grad-

ient of A shown in Koehler and Min (1983) and decreased cyclogenesis

compared with the 20 year average from Whittaker and Horn (1981)

appear consistent with the greatly reduced North American K maximum.

The most striking feature of summer is the signature of the Indian

monsoon.

(6) Ratios of K to A using exact A show the ratio highest in

winter and lowest in summer. This is the reverse of that found

using approximate A. A lower ratio of K to approximate A between

Peixoto and Oort (1974) and this study seems related to domain and

interpolation differences as well as yearly variability.

(7) Spectral analysis produced strong periodicity in K_E at

14 and 16 days. This confirmed earlier results obtained from

visual inspection. Cross spectral analysis of K_Z and K_E revealed

highly significant coherence at 14 days with K_E leading K_Z by 5.25

days. The strong 24 day cycle found by McGuirk and Reiter (1976)

in nearly ten years of data was not evident in any of the K or A

time series. This would seem to indicate the FGGE year was quite

different.

This study has raised some interesting points for future in-

vestigation. The relationship between K, A and cyclones should be

explored further. A study involving a limited region of strong
FGGE cyclone activity might reveal more concrete links between
cyclones and their energy fields. Comparisons between the winter
and spring season off the east coast of North America could add in-
sight into the large seasonal change in this region. Additionally,
time series analysis of twice daily energy quantities at selected
grid points, in latitude bands or summed over limited regions might
reveal more about the periodicities discussed here on a hemispheric
scale.

APPENDIX A

This appendix briefly discusses the procedure used to calculate
the area of grid squares, and those used to perform the vertical
integration.

The area of grid squares is determined by integration of the
equation

$$ds = a^2 \cos \phi \, d\phi d\lambda \qquad (A1)$$

where a is the mean radius of the earth, ϕ is latitude and λ is
longitude. Integration of Equation A1 gives

$$s = a^2 \sin\phi \Big|_{\phi_S}^{\phi_N} \Delta\lambda = a^2 \frac{\sin\phi}{\Delta\phi} \Big|_{\phi_S}^{\phi_N} \Delta\lambda\Delta\phi \qquad (A2)$$

ϕ_N and ϕ_S are the north and south latitude limits of a grid square.
For calculations here, ϕ_N and ϕ_S are 5° apart. $\Delta\phi$ and $\Delta\lambda$ are also
5°. The term $\sin \phi/\Delta\phi$ constitutes the map factor. This method of
area calculation provides an exact determination of the grid square
area because it results from the direct integration of Equation A1.
This method is more accurate than one method which uses the average
of the cosine of the north and south latitudes $(\overline{\cos \phi})$, and another
which uses the cosine of the average of the north and south lati-
tude $(\cos \overline{\phi})$.

Vertical integration of the kinetic energy equations for each
grid square is performed using the trapezoidal rule. The value of

u, v, and p on two isentropic surfaces separated by $\Delta\theta = 10K$ is shown in Figure A1. The upper and lower values of the component winds are averaged ($\hat{u}^\theta = (u_u + u_L)/2$, etc.) while Δp is given by $\Delta p = p_L - p_u$. This gives layer average wind speeds and a mass increment. This procedure is performed over the domain from as low as 220K to 370K. Summation over the actual number of vertical layers yields units of energy per unit area (Jm^{-2}) for the grid square. This value can then be divided by the mass of the atmosphere in the domain of integration to yield specific units (Jkg^{-1}).
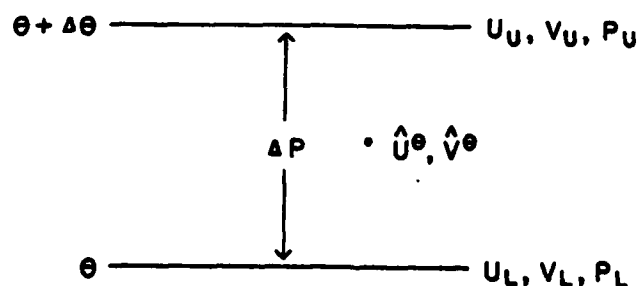
Figure A1. Schematic of interpolation of layer mean quantities
            used in vertical integration. Subscripts refer
            to quantities at θ surface data levels. Δp is pressure
            difference for layer, and $\hat{u}^\theta$ and $\hat{v}^\theta$ are layer average
            winds.

APPENDIX B

This appendix briefly discusses the procedures employed prior to spectral analysis of kinetic energy and available potential energy time series.

A fast Fourier transform (FFT) routine available at the Madison Academic Computing Center (see MACC, 1973) and based on the Cooley and Tukey (1965) algorithm was employed. Prior to using the FFT, certain requirements must be satisfied. For example, there must be no missing values in the series. Consequently, the time series gaps (730 periods - 699 available = 31 gaps) were filled by linear interpolation of values from the nearest available adjacent time periods on each side of the missing period. This resulted in a time series of length 730. Next, factoring requirements for the FFT routine must be met. Since 728 was a convenient number of data periods that met the factoring requirements, the last two time periods were arbitrarily dropped. These remaining 728 periods were subjected to a binomial filter of weights .25/.50/.25 (Hanning filter) to reduce diurnal variability which was found to be large by Koehler and Min (1983) for values of Ae. Although diurnal changes were small for K quantities, it was decided to process all the time series in the same manner.

Because the FGGE period is of finite length, certain adjustments must still be made. For computational purposes, an FFT assumes a time series can be wrapped back on itself in a differen-

tiably well behaved manner. To ensure the beginning and end of a series meet correctly, the series mean is removed and the first and last 1/10th of the series is subjected to a cosine taper consisting of a left- and right-half cosine bell (see Bingham et al., 1967). This process reduces leakage: a problem whereby a pure wave of given frequency is represented by a number of frequencies after transformation. Finally, the series is standardized. This ensures that the variance sums to one and allows spectral estimates at each frequency to be readily interpreted in terms of % variance explained. For additional information on the above procedures, see Bergland (1969), and references therein, Bendat and Piersol (1971) and Bloomfield (1976). Two specific applications to meteorology are found in Madden and Julian (1971) and Julian (1971).

APPENDIX C

This appendix shows the spectral variance plots for exact and

approximate available potential energy. In addition, coherence

plots are presented to show the results of cross spectral analysis.

In each pair of coherence plots, exact A quantities appear in the

top diagram while approximate A quantities are shown below for

comparison. As discussed in Chapter 5, the dashed lines at .815 and

.713 are the significant levels of 1% and 5%. Interpretation of

these figures is left to the reader.
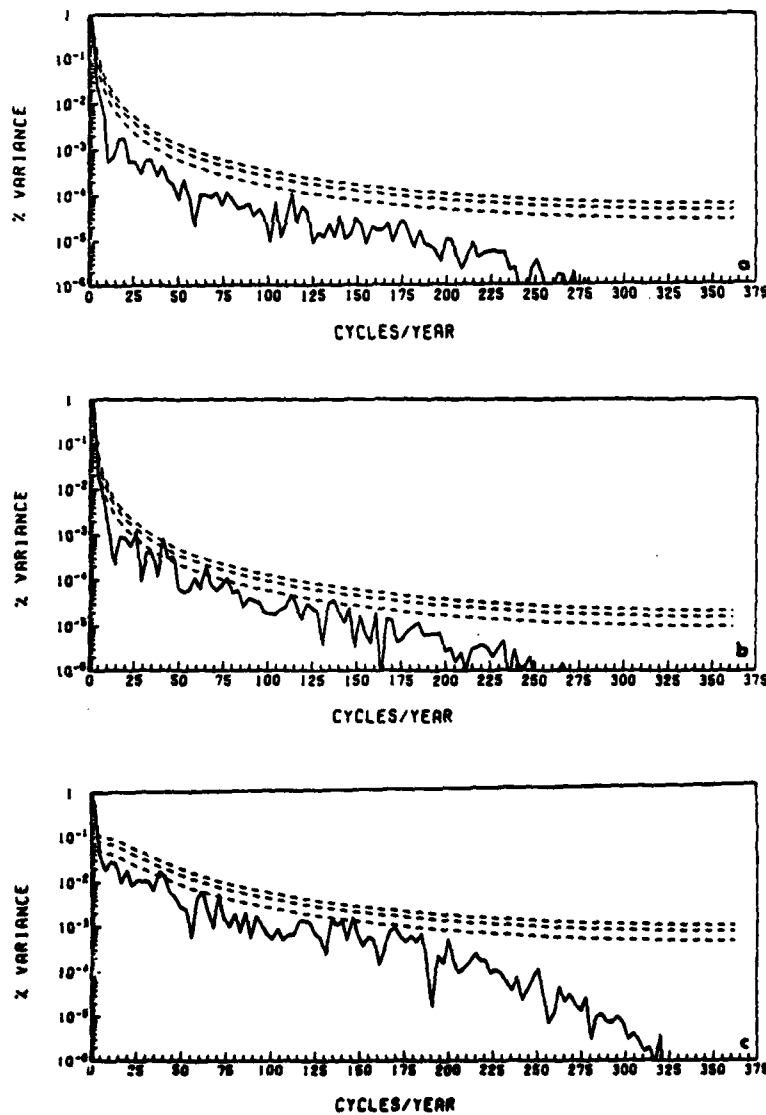
Figure C1. Power variance spectrum for exact A. Expressed as percent variance explained. Dashed lines are confidence limits of 90, 99 and 99.9%. a) A. b) A_Z. c) A_E.
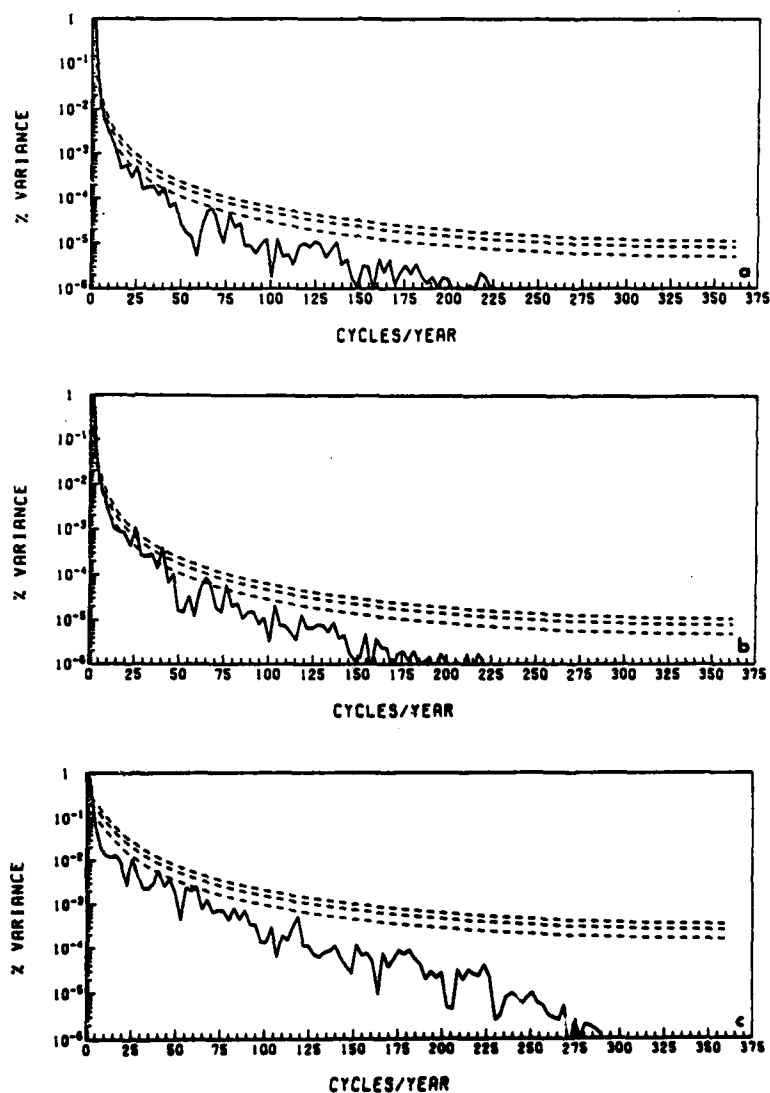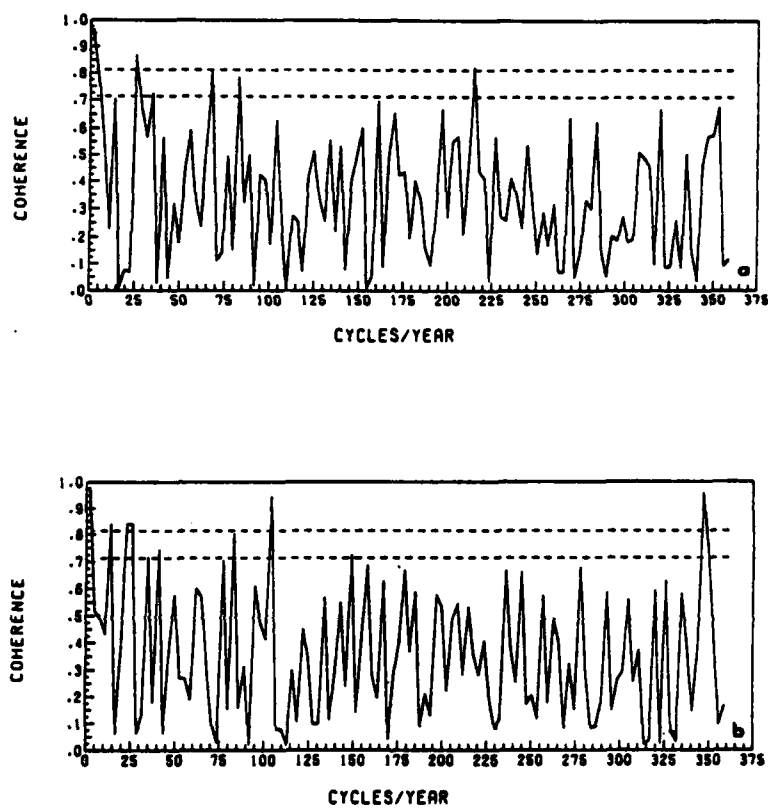
Figure C2. Same as C1 except for approximate A.

Figure C3. Coherence from cross spectral analysis of A and K.
Dashed lines are 1% and 5% significant levels.
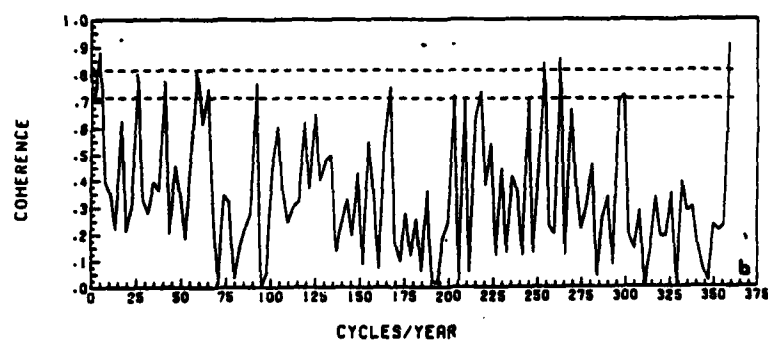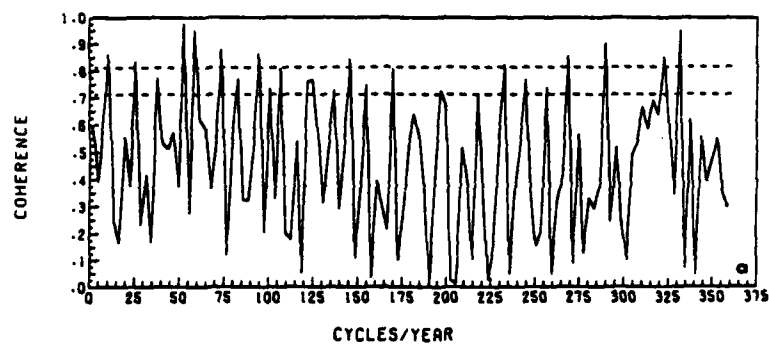a) Exact A and K. b) Approximate A and K.

Figure C4. Same as C3 except A_Z and A_E.   a) Exact A_Z and A_E.
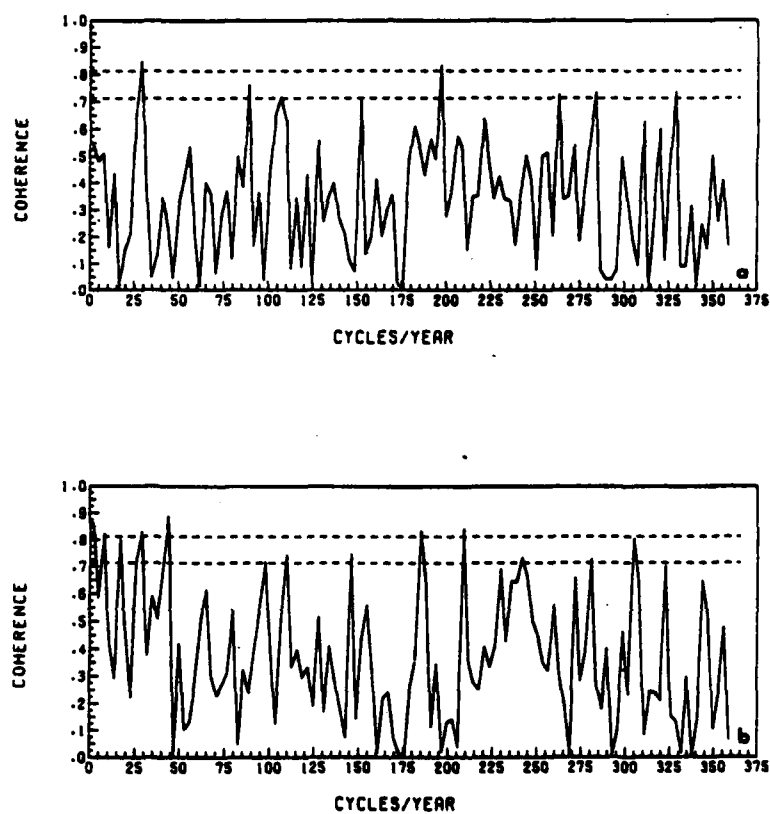b) Approximate A_Z and A_E.

Figure C5. Same as C3 except A_E and K_E.   a) Exact A_E and K_E.
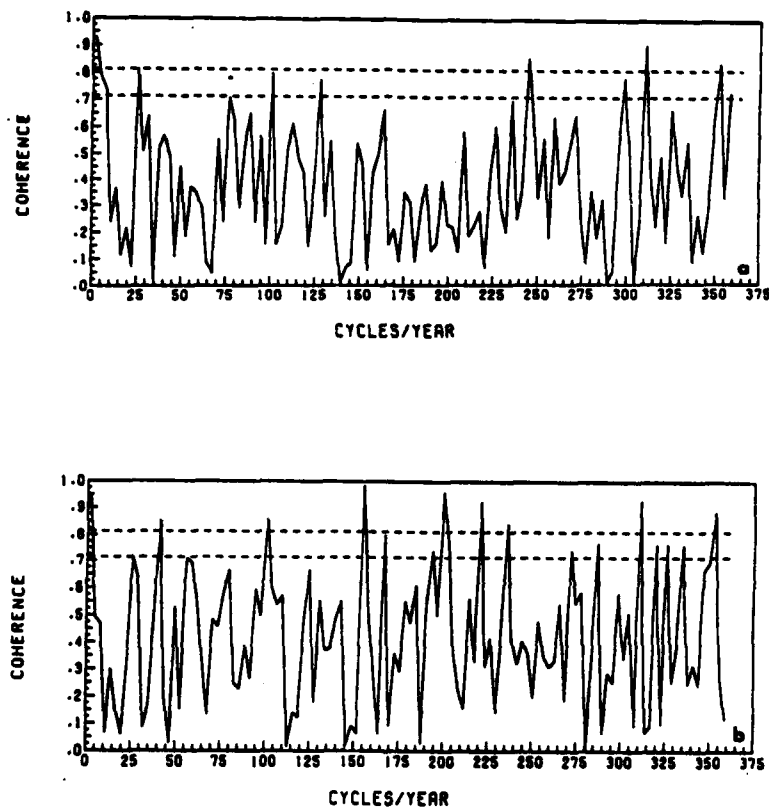b) Approximate A_E and K_E.

Figure C6. Same as C3 except A_Z and K_Z. a) Exact A_Z and K_Z.
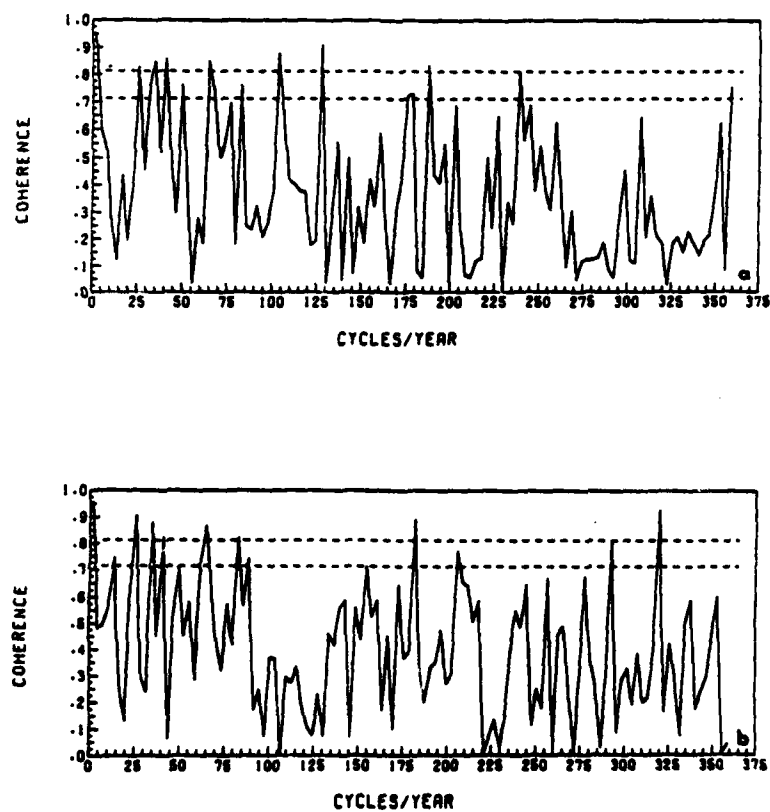b) Approximate A_Z and K_Z.

Figure C7. Same as C3 except A_Z and K_E. a) Exact A_Z and K_E. b) Approximate A_Z and K_E.
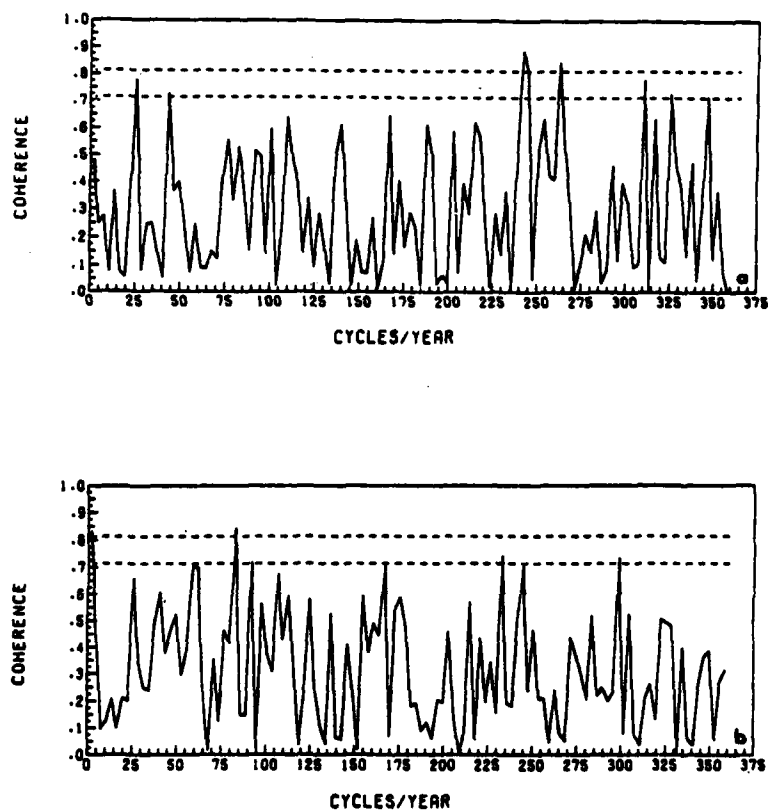
Figure C8. Same as C3 except A_E and K_Z.   a) Exact A_E and K_Z.
            b) Approximate A_E and K_Z.

BIBLIOGRAPHY

Bendat, J.S. and A.G. Piersol, 1971: Random Data: Analysis and
    Measurement Procedure. John Wiley & Sons, Inc., New York,
    407 pp.

Bergland, G.D., 1969: A guided tour of the fast Fourier transform.
    I.E.E.E. Spectrum, 6, 7, 41-52.

Bergman, K.H., 1979: A multivariate optimum interpolation analysis
    system of temperature and wind fields. Mon. Wea. Rev., 107,
    1423-1444.

Bingham, C., M.D. Godfrey and J.W. Tukey, 1967: Modern techniques
    of power spectrum estimation. I.E.E.E. Trans. Audio and
    Electroacoustics, AU-15, 2, 56-66.

Bjorheim, K., P. Julian, M. Kanamitsu, P. Kallberg, P. Price,
    S. Tracton and S. Uppala, 1981: The Global Weather Experiment:
    Daily Global Analyses, December 1978-February 1979. Global
    Atmospheric Research Program, European Centre for Medium Range
    Weather Forecasts.

Bloomfield, P., 1976: Fourier Analysis of Time Series: An Intro-
    duction. John Wiley & Sons., Inc., New York, 258 pp.

Cooley, J.W. and J.W. Tukey, 1965: An algorithm for the machine
    computation of complex Fourier series. Math. Comp., 19,
    297-301.

Crutcher, H.L. and J.M. Meserve, 1970: Selected level heights,
    temperatures and dew points for the Northern Hemisphere.
    NAVAIR 50-1C-52, Naval Weather Service Command, Washington, D.C.,
    U.S. Government Printing Office.

Dickson, R.R., 1979: Weather and circulation of February 1979.
    Mon. Wea. Rev., 107, 624-630.

Dickson, R.R., 1980: Weather and circulation of November 1979. Mon.
    Wea. Rev., 108, 226-231.

Flattery, T.W., 1970: Spectral models for global analysis and fore-
    casting. Proceedings of the Sixth AWS Technical Exchange Confer-
    ence, U.S. Naval Academy, Annapolis, Maryland, Air Weather
    Service Technical Report 242, 42-54.

Fleming, R.J., T.M. Kaneskige and W.E. McGovern, 1979a: The Global Weather Experiment I. The observational phase through the first special observing period. *Bull. Am. Meteorol. Soc.*, 60, 649-659.

Fleming, R.J., T.M. Kaneskige, W.E. McGovern and T.E. Bryan, 1979b: The Global Weather Experiment II. The second special observing period. *Bull. Am. Meteorol. Soc.*, 60, 1316-1322.

Julian, P.R., 1971: Some aspects of variance spectra of synoptic scale tropospheric wind components in mid latitudes and in the tropics. *Mon. Wea. Rev.* 99, 12, 954-965.

Klein, W.H., 1957: *Principal tracks and mean frequencies of cyclones and anticyclones in the Northern Hemisphere*. Res. Pap. No. 40, U.S. Weather Bureau, U.S. Government Printing Office, Washington, D.C., 60 pp.

Koehler, T.L. and K.D. Min, 1983: Available potential energy and extratropical cyclone activity during the FGGE year. *Tellus*, in press.

Madden, R.A. and P.R. Julian, 1971: Detection of a 40-50 day oscillation in the zonal wind in the tropic Pacific. *J. Atmos. Sci.*, 28, 7, 702-708.

Madison Academic Computing Center.(MACC), 1973: *Fourier Transform Routines*, University of Wisconsin-Madison.

McGuirk, J.P. and E.R. Reiter, 1976: A vacillation in atmospheric energy parameters. *J. Atmos. Sci.*, 33, 11, 2079-2093.

McPherson, R.D., K.H. Bergman, R.E. Kistler, G.E. Rasch and D.S. Gordon, 1979: The NMC operational global data assimilation system. *Mon. Wea. Rev.*, 107, 1445-1461.

Miller, A.J., 1974: Periodic variation of atmospheric circulation at 14-16 days. *J. Atmos. Sci.*, 31, 3, 720-726.

Min, K.D., 1981: Available potential energy in the Northern Hemisphere during the FGGE year. *Ph.D. Thesis*, Department of Meteorology, University of Wisconsin-Madison, 114 pp.

Min, K.D. and L.H. Horn, 1982: Available potential energy in the Northern Hemisphere during the FGGE year. *Tellus*, 34, 526-539.

Mitchell, J.M., chrm., 1966: *Climatic Change*. WMO Tech. Note No. 79, World Meteorological Organization, Geneva, 79 pp.

Olson, J.G., 1982: The relationship between the 20-year mean (1958-77) 500 mb geostrophic wind, cyclogenesis, and cyclone frequency over the Northern Hemisphere. M.S. Thesis, Department of Meteorology, University of Wisconsin-Madison, 63 pp.

Oort, A.H., 1964: On the estimates of the atmospheric energy cycle. Mon. Wea. Rev., 92, 483-493.

Oort, A.H. and J.P. Peixoto, 1974: The annual cycle of the energetics of the atmosphere on a planetary scale. J.G.R., 79, 18, 2705-2719.

Oort, A.H. and J.P. Peixoto, 1976: On the variability of the atmospheric energy cycle within a 5-year period. J.G.R., 81, 21, 3643-3659.

Panofsky, H.A. and G.W. Brier, 1958: Some Applications of Statistics to Meteorology. The Pennsylvania State University, University Park, PA, 224 pp.

Peixoto, J.P. and A.H. Oort, 1974: The annual distribution of atmospheric energy on a planetary scale. J.G.R., 79, 15, 2149-2159.

Saltzmann, B., 1970: Large-scale atmospheric energetics in the wave number domain. Rev. Geophys. Space Phys., 8, 2, 289-302.

Smith, P.J., 1980: The energetics of extratropical cyclones. Rev. Geophys. Space Phys., 18, 2, 378-386.

Taubensee, R.E., 1979: Weather and circulation of December 1978. Mon. Wea. Rev., 107, 354-360.

Tomatsu, K., 1979: Spectral energetics of the troposphere and lower stratosphere. Adv. Geophys., 21, 289-405.

Townsend, R.D., 1980: A diagnostic study of the zonally-averaged global circulation in isentropic coordinates. Ph.D. Thesis, Department of Meteorology, University of Wisconsin-Madison, 221 pp.

Wagner, A.J., 1979: Weather and circulation of January 1979. Mon. Wea. Rev., 107, 499-506.

Whittaker, L.M., 1983: (Personal communication), Department of Meteorology, University of Wisconsin-Madison.

Whittaker, L.M. and L.H. Horn, 1981: Geographical and seasonal distribution of North American cyclogenesis, 1958-1977. _Mon. Wea. Rev._, 109, 2312-2322.

Whittaker, L.M. and L.H. Horn, 1982: _Atlas of Northern Hemisphere Extratropical Cyclone Activity, 1958-1977_, Department of Meteorology, University of Wisconsin-Madison, 67 pp.

END

DATE
FILMED

1 84

DTIC